

Non-Gaussian Error Bars in Galaxy Surveys (Part 1)

Joachim Harnois-Déraps^{1,2} \star and Ue-Li Pen¹ \dagger

¹Canadian Institute for Theoretical Astrophysics, University of Toronto, M5S 3H8, Canada

²Department of Physics, University of Toronto, M5S 1A7, Ontario, Canada

19 March 2012

ABSTRACT

We propose a method to estimate non-Gaussian error bars on the matter power spectrum from galaxy surveys in the presence of non-trivial survey selection functions. The estimators are often obtained from formalisms like FKP and PKL, which rely on the assumption that the underlying field is Gaussian. The Monte Carlo method is more accurate but involves the tedious process of running and cross-correlating a large number of N-body simulations, in which the survey volume is embedded. From 200 N-body simulations, we extract a non-linear covariance matrix as a function of two scales and of the angle between two Fourier modes. All the non-Gaussian features of that matrix are then simply parameterized in terms of a few fitting functions and Eigenvectors. We furthermore develop a fast and accurate strategy that combines our parameterization with a general galaxy survey selection function, and incorporate non-Gaussian Poisson uncertainty. We describe how to incorporate these two distinct non-Gaussian contributions into a typical analysis pipeline, and apply our method with the selection function from the 2dFGRS. We find that the observed Fourier modes correlate at much larger scales than that predicted by both FKP formalism or by pure N-body simulations in a ‘top hat’ selection function. In particular, the observed Fourier modes are already 50 per cent correlated at $k \sim 0.1 h\text{Mpc}^{-1}$, and the non-Gaussian fractional variance on the power spectrum ($\sigma_P^2/P^2(k)$) is about a factor of 3.0 larger than the FKP prescription. At $k \sim 0.4 h\text{Mpc}^{-1}$, the deviations are an order of magnitude.

Key words: Large scale structure of Universe – Surveys – Dark matter – Distance Scale – Cosmology : Observations – Methods: data analysis

1 INTRODUCTION

With new galaxy surveys probing a larger dynamical range of our Universe, our ability to constrain cosmological parameters is improving considerably. In particular, one of the most important goal of modern cosmology is to understand the nature of dark energy (Albrecht et al. 2006), a challenging task since there are currently no avenues for direct observations. It is however possible to probe its dynamics via its equation of state ω , which enters in the Friedmann equation that governs the expansion of the Universe. Among different ways ω can be measured, the detection of the baryonic acoustic oscillations (BAO) dilation scale (Eisenstein et al. 2005; Tegmark et al. 2006; Hütsi 2006; Percival et al. 2007; Blake et al. 2011) is one of the favourite, both because of the low systematic uncertainty and the potentially high statistics one can achieve with current (Huchra et al. 1990; York et al. 2000; Colless et al. 2003; Drinkwater et al. 2010) and future galaxy surveys (Peterson et al. 2006; Acquaviva et al. 2008; Schlegel et al. 2009; LSST Science Collaborations et al. 2009; Benítez et al. 2009; Beaulieu et al. 2010).

The strength of the BAO technique relies on an accurate and precise measurement of the matter power spectrum, whose uncertainty propagates on to the dark energy parameters via a Fisher matrix (Tegmark 1997). It is thus of the utmost importance to have optimal estimators of both the mean and the uncertainty of the power spectrum to start with. The prescription to construct an estimator for the power spectrum of a Gaussian random field, in a given galaxy survey, was pioneered by Feldmann, Kaiser and Peacock (Feldman et al. 1994) (FKP for short). It states that the survey selection function effectively couples Fourier bands that are otherwise independent, and that the underlying power should then be deconvolved (Sato et al. 2011). This technique has been used in many power spectrum measurement (Feldman et al. 1994; Percival et al. 2001; Cole et al. 2005; Hütsi 2006; Blake et al. 2010). Although it is fast, the error bars between the bands are correlated, plus it has the undesired tendency to smear out the underlying power spectrum, which can effectively reduce the signal-to-noise ratio in a BAO measurement. In that sense, the FKP power spectrum is said to be *suboptimal*.

The band correlation induced by the FKP prescription can be removed by an Eigenvector decomposition of the selection function, following the Pseudo Karhunen-Loève formalism (Vogele & Szalay 1996)(PKL). This was used in the analysis of the SDSS data

\star E-mail: jharno@cita.utoronto.ca

\dagger E-mail: pen@cita.utoronto.ca

(Tegmark et al. 2006) and is the most optimal (i.e. loss-less) estimator for Gaussian random field, as understood from the information theory point of view. It is nevertheless a well known fact that this Gaussian assumption about the field is only valid in the linear regime, since the non-linear gravitational collapse of the density effectively couples different Fourier modes together (Meiksin & White 1999; Rimes & Hamilton 2005), and the phases of the modes are no longer random (Coles & Chiang 2000). Both the FKP and PKL prescriptions, by their Gaussian treatment, do not take into account the intrinsic non-linear coupling of the Fourier modes. It follows from this that for both methods, the measured power spectrum is suboptimal and the error bars are systematically biased. Although the bias is usually small, it causes a problem when estimating derived quantities that need to be measured with per cent level accuracy.

For instance, the observed BAO signal sits right at the transition between the linear and the non-linear regime, therefore an optimal estimator of the power spectrum must incorporate the non-linear modes. In particular, constraints on dark energy from BAO measurements require an accurate measurement of the matter power spectrum covariance matrix. Under the FKP and PKL formalisms, the covariance matrix is biased as it tends to underestimate the uncertainty and the amount of correlation between the power bands. Alternative ways of estimating the error, i.e. methods that involve mock catalogues, do model these non-linear dynamics, but it is not clear that the results are precise enough to measure four-points statistics, and we rather rely on accurate N-body simulations.

Even more relevant is the recent realization that an optimal, i.e. non-Gaussian, estimate of the BAO dilation scale requires a precise measurement of the *inverse* of the matrix, which is challenging due the noisy nature of the forward matrix. It was nevertheless shown that, by consistency, the error bars on a suboptimal measurement of the power spectrum should be calculated in a manner that incorporates some noise in the measurement of the mean (Ngan et al. 2011). Only an optimal measurement of the mean power spectrum can be matched with the straightforward (i.e. noise-less) non-linear covariance matrix, and it was shown in the same paper that both estimators differ by a few percent.

When constructing an estimator of the covariance matrix that corresponds to the sensitivity of a particular survey, the convolution with the survey selection function is one of the most challenging part. Whereas the convolution of the underlying power spectrum can be operated with angle averaged quantities, the convolution of the covariance matrix must be done in 6 dimensions, since the underlying covariance is not isotropic: Fourier modes with smaller angular separations are more correlated than those with larger angles (Chiang et al. 2002; Bernardeau et al. 2002). The first challenge is to measure accurately this angular correlation, which is also scale dependent. Neither second order perturbation theory nor log-normal densities have been shown to calculate this quantity accurately, we must therefore rely on N-body simulations. This requires a special approach, since a naive pair counting of all Fourier modes in the four-point function, at a given angle, would take forever to compute. The second challenge comes from the 6-dimensional convolution of the covariance matrix with the survey function. This is a task that current computer clusters cannot solve by brute force, so we must find a way to use symmetries of the system and reduce the dimensionality of the integral. The fact is that the underlying covariance really depends only on three variables: two scales and the relative angles between the two Fourier modes. Moreover, it turns out, as we describe in section 6, that it is possible to express this

matrix into a set of multipoles, each of which can further be decomposed into a product of Eigenvectors. This effectively factorizes the three dimensions of the covariance, hence the convolution can be broken down into smaller pieces. By doing so, the non-Gaussian calculation is within reach, and we present in this paper the first attempt at measuring deviations from Gaussian calculations, including both Poisson noise and a survey selection function. In short, the main ideas of this paper can be condensed as follow:

- (i) The underlying non-linear covariance matrix of the matter power spectrum exhibits many non-Gaussian features in the trans- and non-linear regimes. First, the diagonal elements of the angle-averaged covariance grow stronger, and correlation across different scales becomes important. Second, Fourier modes with similar (or identical) magnitudes correlate more if the angle between them is small.
- (ii) It is possible to model all of the aboved mentioned non-Gaussian aspects with a small number of simple functions.
- (iii) With such a parameterization, it is possible, for the first time, to solve the six-dimensional integral that enters the convolution of the covariance of the power spectrum with the galaxy survey selection function.

Concerning the second point, the parameters that best fit our measurements are provided in section 7, but these are separately testable, and could be verified by other groups and in other ways. These are anyway expected to change when one uses haloes instead of particles. The third point is, however, a straightforward recipe that is robust under possible changes of best-fitting parameters, and provides, assuming that the input parameters are correct, an unbiased measurement of the non-Gaussian uncertainty of the matter power spectrum.

Our first objective is thus to measure the covariance of the power spectrum between various scales and angles, and organize this information into a compact matrix, $C(k, k', \theta)$. We describe how we solve this problem in a fast way, which is based on a series of fast Fourier transforms that can be run in parallel on a large number of computers. We find that the angular dependence, at fixed scales ($k \neq k'$), is rather smooth, it agrees with analytical predictions in the linear regime, but deviates importantly from Gaussianity for smaller scales. The dependence is somehow similar when the two scales are identical, up to a delta function for vanishing angles. We also found that, once projected on to a series of Legendre polynomials, it takes very few multipoles to describe the complete original function. We perform this transform for all scale combinations and group the results in terms of multipole moments.

Our second objective is to provide a general method to combine this $C(k, k', \theta)$ with a survey selection function and non-Gaussian Poisson noise, and hence allow the extraction of non-Gaussian error bars on the measured power spectrum. We test our technique on the publicly available 2dFGRS selection functions (Norberg et al. 2002) and find that there is a significant departure between the Gaussian and non-Gaussian treatment. In particular, the fractional error of the power spectrum ($\sigma_p^2/P^2(k)$) at $k \sim 0.1h\text{Mpc}^{-1}$ is about a factor of 3.0 higher in the non-Gaussian analysis, and the departure reaches an order of magnitude by $k \sim 0.4h\text{Mpc}^{-1}$. The method proposed here can be also applied to other kinds of BAO experiments, including intensity mapping from the emission of the 21 cm line by neutral Hydrogen (Peterson et al. 2006; Lazio 2008; Schlegel et al. 2009), or Lyman- α forests surveys (McDonald & Eisenstein 2007; McQuinn & White 2011). We did not, however, include the effect of redshift distortions, and focused our efforts on dark matter density fields obtained from sim-

ulated particles. An improved version of this work would include both of these effects, however.

As indicated by the title, this paper is the first part of a general strategy that aims at constructing unbiased, non-Gaussian estimators of the uncertainty on the matter power spectrum measured in galaxy surveys. The second part, which we hereafter refer to as HDP2 (in preparation), exploits the fact that the measurement of the $C(k, k', \theta)$ matrix provides a novel handle at measuring $C(k, k')$: the two quantities are related by a straightforward integration over θ . As shown in a later section of the current paper, it turns out that the main contributions to $C(k, k')$ come from small angles, while larger angles are noise dominated. It is thus possible to perform a noise weighted integral, which results in a more optimal measurement of $C(k, k')$ and of its error bars, compared to direct or bootstrap sampling. We can then extract accurate non-Gaussian error bars on the power spectrum with fewer realizations, which opens the door for an error estimate directly from the data (i.e. an internal estimate), a significant step forward in the error analysis of galaxy surveys.

The current paper is organized as follow: in section 2, we briefly review the FKP method, and describe how to estimate non-Gaussian error bars in realistic surveys, given a previous knowledge of $C(k, k', \theta)$. We then lay down the mathematical formalism that describes how we extract this quantity from simulated density fields in section 3. Section 4 describes sanity checks, null tests, and our N-body simulations. We present our measurements of $C(k, k', \theta)$ in section 5, and describe the multipole decomposition in section 6. In section 7, we further simplify the results by extracting the principal Eigenvectors and provide fitting formulas to reconstruct easily the full covariance matrix. Section 8 contains results of applying our method for a set of simple selection functions. We finally discuss some implications and extensions of our methods in section 9, and conclude in section 10.

2 MATTER POWER SPECTRUM FROM GALAXY SURVEYS

In this section, we quickly review the general FKP method, which is commonly used in data analysis (Feldman et al. 1994; Percival et al. 2001; Blake et al. 2010). We then point out some of the major flaws of such techniques when measuring the uncertainty, and describe how non-Gaussian error bars could be estimated in principle. Before moving on, though, we first lay down the conventions used throughout the paper. The reader familiar with the FKP method may skip to section 2.2.

A continuous density field $\delta(\mathbf{x})$ is related to its Fourier transform $\delta(\mathbf{k})$ by

$$\delta(\mathbf{k}) = \int \delta(\mathbf{x}) e^{i\mathbf{k}\cdot\mathbf{x}} d^3x \quad (1)$$

where \mathbf{k} is the wave number corresponding to a given Fourier mode. The power spectrum $P(\mathbf{k})$ of the field is defined as:

$$\langle \delta(\mathbf{k}) \delta^*(\mathbf{k}') \rangle = (2\pi)^3 P(\mathbf{k}) \delta_D(\mathbf{k} - \mathbf{k}') \quad (2)$$

and is related to the mass auto-correlation function by :

$$\xi(\mathbf{x}) = \frac{1}{(2\pi)^3} \int e^{-i\mathbf{k}\cdot\mathbf{x}} P(\mathbf{k}) d^3k \quad (3)$$

In the above expressions, the angle brackets refer to a volume average in Fourier space, and $\delta_D(\mathbf{k})$ stands for the Dirac delta function.

2.1 The optimal estimator of the power spectrum

The power spectrum of the matter field contains a wealth of information about the cosmic history and the principal constituents of the Universe. Unfortunately, it is not directly detectable, since our observations are subject to cosmic variance, detection noise, light to mass bias, redshift distortions and incomplete sky surveys. The FKP method provides an optimal estimator of the matter power spectrum $P(k)$ under the assumption that the density field is Gaussian. It is formulated in terms of the survey selection function $W(\mathbf{x})$, the galaxy number density n , the dimensions (n_x, n_y, n_z) of the grid where the Fourier transforms are performed, and the actual number count per pixel $n(\mathbf{x})$. All the following calculations can be found in Feldman et al. (1994), and are included here for the sake of completeness.

The first step is to construct series of weights $w(\mathbf{x})$ as

$$w(\mathbf{x}) = \frac{1}{1 + W(\mathbf{x})N_c n P_0} = \frac{1}{1 + \bar{n}P_0} \quad (4)$$

where $N_c = n_x n_y n_z$, \bar{n} is the mean galaxy density and P_0 is a characteristic amplitude of the power spectrum at the scale we want to measure. Since the latter is not known *a priori*, it is usually obtained from a theoretical model, and sometimes updated iteratively. The selection function is also normalized such that $\sum_{\mathbf{x}} W(\mathbf{x}) = 1$.

The optimal estimator of the power spectrum, $P_{est}(\mathbf{k})$, is obtained first by re-weighting each pixel by the weights in [Eq. 4], then by subtracting from the result a random catalogue with the same selection function, weights and number of objects N . After taking the expectation value of the results, the 2-points statistics of the pixel counts becomes

$$\langle n(\mathbf{x})n(\mathbf{x}') \rangle = \bar{n}\bar{n}'(1 + \xi(\mathbf{x} - \mathbf{x}')) + \bar{n}\delta_D(\mathbf{x} - \mathbf{x}') \quad (5)$$

where \bar{n} is the mean density in the patch over which the average is performed. The Fourier transform is then given by

$$\langle P_{est}(\mathbf{k}) \rangle = \frac{|n(\mathbf{k}) - NW(\mathbf{k})|^2 - N \sum_{\mathbf{x}} W(\mathbf{x})w^2(\mathbf{x})}{N^2 N_c \sum_{\mathbf{x}} W^2(\mathbf{x})w^2(\mathbf{x})} \quad (6)$$

where denominator is a convenient normalization. This measured power is aliased by the grid mass assignment scheme, and should be divided by the appropriate function (Jing 2005).

What this estimator measures is not the underlying power spectrum $P(k)$, but a convolution with the survey selection function:

$$\langle P_{est}(\mathbf{k}) \rangle = \frac{\sum_{\mathbf{k}'} P(\mathbf{k}') |W(\mathbf{k} - \mathbf{k}')|^2}{N_c \sum_{\mathbf{x}} W^2(\mathbf{x})w^2(\mathbf{x})} \quad (7)$$

It ideally needs to be deconvolved, an operation that is not always possible.

For many survey geometries, the convolution effectively transfers power across different bins which are uncoupled to start with (Tegmark et al. 2006). As mentioned previously, the PKL prescription also assumes that the density field is Gaussian, but rotates into a basis in which the bins are decoupled. In that sense, the PKL technique is more optimal than the FKP, unless the selection function is close to a ‘‘top hat’’, in which case the induced mode coupling vanishes. Both case, however, rely on the fundamental assumption that the underlying density field is Gaussian, which is known to be inaccurate in the trans- and non-linear regime, where one still wants an accurate measure of the power spectrum for a BAO analysis. Obtaining accurate error bars is a requirement for optimal analyses, and we shall examine how these are usually obtained.

2.2 The FKP covariance matrix

The covariance matrix of the angle averaged power spectrum is a four point function that contains the information about the band error bars, and possible correlation between them. As mentioned earlier, it is required for many cosmological parameter studies. It is generally obtained from the power spectrum as

$$C(k, k') = \langle \Delta P(k) \Delta P(k') \rangle \quad (8)$$

where $\Delta P(k)$ refers to the fluctuations of the measured values about the mean, which is ideally obtained from averaging over many realizations. In a typical galaxy survey, such independent realizations are obtained by sampling well separated patches of the sky. Because of the cost of such an operation, the number of patches is usually very small. The covariance matrix is thus not resolved from the data, and the error bars are obtained with external techniques, i.e. from mock catalogues¹, or directly from Gaussian statistics (see HDP2 for a prescription that overcomes this challenge). For a uniform (top-hat) selection function, the Gaussian covariance matrix is estimated as:

$$C^{Gauss}(k, k') = \frac{2}{N(k)} (P(k) + P_{shot})^2 \delta_{kk'} \quad (9)$$

where $P_{shot} = 1/n$ and $N(k)$ is the number of Fourier modes that enters in the measurement of $P(k)$. In the ideal scenario of perfect spherical symmetry and resolution, $N(k) = 4\pi k^2 \Delta k \left(\frac{1}{2\pi}\right)^3$, with Δk being the width of the k -band. The Kronecker delta function ensures that there is no correlation between different modes, an inherent property of Gaussian random fields. This equation can easily be modified to deal with measurements without angle averaging.

The FKP prescription provides a generalization of [Eq. 9] for the case where the selection function varies across the volume. It is obtained from [Eq. 6] and given by

$$C^{FKP}(\mathbf{k}, \mathbf{k}') = \frac{2}{N(\mathbf{k})N(\mathbf{k}')} \sum_{\mathbf{k}, \mathbf{k}'} |PQ(\mathbf{k} - \mathbf{k}') + S(\mathbf{k} - \mathbf{k}')|^2 \quad (10)$$

where

$$Q(\mathbf{k}) = \frac{\sum_{\mathbf{x}} W^2(\mathbf{x}) w^2(\mathbf{x}) \exp(i\mathbf{k}\mathbf{x})}{\sum_{\mathbf{x}} W^2(\mathbf{x}) w^2(\mathbf{x})} \quad (11)$$

$$S(\mathbf{k}) = \left(\frac{1}{nN_c} \right) \frac{\sum_{\mathbf{x}} W(\mathbf{x}) w^2(\mathbf{x}) \exp(i\mathbf{k}\mathbf{x})}{\sum_{\mathbf{x}} W^2(\mathbf{x}) w^2(\mathbf{x})} \quad (12)$$

In [Eq. 10], P is taken to be the mean of the power spectrum at separation $\mathbf{k} - \mathbf{k}'$. Because the selection functions are usually quite compact about $\mathbf{k} = 0$, that approximation is reasonable for Gaussian fields. Also, [Eq.9] can be recovered by setting $W(\mathbf{x}) = 1/N_c$.

2.3 Non-Gaussian error bars

As mentioned in the last section, it is necessary to have access to many realization of the matter field in order to measure a non-Gaussian covariance matrix of power spectrum. This could in principle be done from data across many different patches in the sky, but even then, we have only one sky to resolve the largest modes, which would therefore be dominated by cosmic variance. Not to mention the cost and time involved in measuring many large but disconnected volumes. Fortunately, N-body simulations are now accurate and fast enough to generate large numbers of measurements of the

matter power spectrum. Since they model the non-linear dynamics of structure growth, the density fields they generate are non-Gaussian. The covariance matrix constructed from a high number of simulations indeed shows a correlation across different scales in the non-linear regime (Meiksin & White 1999; Rimes & Hamilton 2005; Takahashi et al. 2009; Ngan et al. 2011).

Although much more representative of the underlying covariance, such matrices are hard to incorporate in a data analysis, first because they are based on a fixed set of cosmological parameters, but also because the simulated volume is cubic and periodic. Each survey group typically needs to run at least one N-Body simulation, and measure the power spectrum with and without the measured selection function, in order to quantify the bias of their measurement. The complete approach would then be to run hundreds of these to measure the covariance matrix, and that over a range of cosmological parameters values. This whole procedure is expensive, which explains why it is never done in practice. The alternative is to use mock galaxy catalogues, obtained, for example, from log normalization of Gaussian densities, second order perturbation theory (PT), haloPT, and so on. Unfortunately, the accuracy of such techniques at modelling the four-point functions and angle dependencies has not been fully quantified.

Another artefact of the simulations is that the number of particles can be arbitrarily adjusted such as to suppress the Poisson noise down to a level where it is negligible. This is certainly not true for many galaxy survey, in which the number density is often much lower. We measure a non-Gaussian Poisson error by sampling random fields with a selection threshold chosen as to mimic the number density of a realistic survey, and incorporate the effect manually in the analysis, as explained in section 8.

To measure non-Gaussian error bars on a realistic survey, the most accurate procedure would be to convolve the best available estimator of the covariance matrix with the selection function. Because the later is generally not spherically symmetric, it is the full 6-dimensional covariance matrix, $C(\mathbf{k}, \mathbf{k}')$, that needs to be integrated over. Let us suppose, for a moment, that we successfully measured that complete non-Gaussian covariance matrix. It would first contain an element for each Fourier modes \mathbf{k} (i.e. with no angular averaging), and from [Eq. 7 and 8], we can write:

$$C_{est}(\mathbf{k}, \mathbf{k}') = \frac{\sum_{\mathbf{k}'', \mathbf{k}'''} \langle \Delta P(\mathbf{k}'') \Delta P(\mathbf{k}''') \rangle |W(\mathbf{k} - \mathbf{k}'')|^2 |W(\mathbf{k}' - \mathbf{k}''')|^2}{(N^2 N_c \sum_{\mathbf{x}} W^2(\mathbf{x}) w^2(\mathbf{x}))^2} \quad (13)$$

where the angled bracket is nothing else but that full covariance matrix $C(\mathbf{k}'', \mathbf{k}''')$. We can then simplify the result since the covariance between two Fourier modes depends only on the angle γ between them, and not on the absolute orientation of the pair in space. In other words, we make use of this symmetry argument to write $C(\mathbf{k}'', \mathbf{k}''') = C(k'', k''', \gamma)$ without loss of generality. This angle can further be expressed in terms of the two angles made by \mathbf{k}'' and \mathbf{k}''' as

$$\cos\gamma = \cos\theta'' \cos\theta''' + \sin\theta'' \sin\theta''' \cos(\phi'' - \phi''') \quad (14)$$

We show in a later section of this paper that the true covariance matrix can be decomposed into a sum of factorized terms, each of the form $F_1(k'') F_2(k''') G_1(\theta'', \phi'') G_2(\theta''', \phi''')$. Therefore the double convolution of [Eq. 13] can actually be broken into a sum of smaller pieces, with at most 3-dimensional integrals to perform.

¹ We post-ponne the discussion on mock catalogues until the next section

3 MEASURING THE ANGULAR DEPENDENCE: THE METHOD

As mentioned above, our first objective is to extract the covariance matrix of the power spectra from N-Body simulations, as a function of two scales and one angle: $C(k, k', \theta)$. In this section, we develop a novel way to obtain covariances and cross-correlations and which allows us to perform this measurement.

3.1 Cross-correlations from Fourier transforms

We begin by assuming we have measured the power spectrum from a large number of simulations. We first compute the mean of the angle averages: $\tilde{P}(k) \equiv \langle P(\mathbf{k}) \rangle_{N, \Omega}$ and the deviation from the mean of each mode:

$$\Delta P(\mathbf{k}) = P(\mathbf{k}) - \tilde{P}(k) \quad (15)$$

We then select two scales, k_i and k_j , that we want to cross-correlate. We make two identical copies of three-dimensional power spectra and multiply each one by a radial top hat function corresponding to the particular scales:

$$\Delta P_i(\mathbf{k}) \equiv \Delta P(\mathbf{k}) u_i(|\mathbf{k}|) \quad (16)$$

where $u_i(k) = \theta(k - k_i) \theta(-k + k_i + \delta k)$ is the product of two Heaviside functions. Also, δk is the shell thickness, taken to be very small. We then cross-correlate the subsets and define:

$$\Sigma^{ij}(\Delta \mathbf{k}) = \frac{1}{(2\pi)^3} \int \Delta P_i(\mathbf{k}) \Delta P_j(\mathbf{k} + \Delta \mathbf{k}) d^3 k \quad (17)$$

We then express both $\Delta P_{i,j}(\mathbf{k})$'s in [Eq. 17] in terms of their mass auto-correlation functions $\Delta \xi_{i,j}(\mathbf{x})$. We first integrate over $\exp[i\mathbf{k} \cdot (\mathbf{x} + \mathbf{x}')] d^3 k$ and obtain a delta function, which allows us to get rid of one of the real space integrals. After slightly rearranging the terms, we obtain:

$$\Sigma^{ij}(\Delta \mathbf{k}) = \int \Delta \xi_i(\mathbf{x}) \Delta \xi_j^*(\mathbf{x}) e^{-i\Delta \mathbf{k} \cdot \mathbf{x}} d^3 x \quad (18)$$

In the above equation, $\Delta \xi_i$ can be expressed as:

$$\begin{aligned} \Delta \xi_i(\mathbf{x}) &= \frac{1}{(2\pi)^3} \int e^{-i\mathbf{k} \cdot \mathbf{x}} \Delta P(\mathbf{k}) u_i(|\mathbf{k}|) d^3 k \\ &= \frac{1}{(2\pi)^3} \int_{k_i}^{k_i + \delta k} k^2 dk \int e^{-i\mathbf{k} \cdot \mathbf{x}} \Delta P(\mathbf{k}) d\Omega \end{aligned} \quad (19)$$

Since the shells we select are very thin, we can safely approximate that the power spectrum is constant over the infinitesimal range, and thus perform the k integral:

$$\Delta \xi_i(\mathbf{x}) = \frac{1}{(2\pi)^3} k_i^2 \delta k \int e^{-i\mathbf{k}_i \cdot \mathbf{x}} \Delta P_i(\mathbf{k}) d\Omega \quad (20)$$

We repeat the same procedure for the scale j , multiply both auto-correlation functions together, and Fourier transform the product, following [Eq. 18]. The result is the cross-correlation $\Sigma^{ij}(\Delta \mathbf{k})$, which becomes, after performing the x integral over the plane wave:

$$\Sigma^{ij}(\Delta \mathbf{k}) = \frac{1}{(2\pi)^3} k_i^2 k_j^2 \delta^2 k \int d\Omega \int d\Omega' \times \quad (21)$$

$$\Delta P_i(\mathbf{k}) \Delta P_j(\mathbf{k}') \delta_D(\mathbf{k}' - \mathbf{k}_i - \Delta \mathbf{k}) \quad (22)$$

The delta function enforces $\Delta \mathbf{k}$ to point from \mathbf{k}_i to \mathbf{k}' . This geometry allows us to use the cosine law and relate $|\Delta \mathbf{k}|$ to the angle θ it subtends, as seen in Fig. 1, such that:

$$\theta = \cos^{-1} \left(\frac{k_j^2 + k_i^2 - |\Delta \mathbf{k}|^2}{2k_j k_i} \right) \quad (23)$$

Since many $\Delta \mathbf{k}$ subtend the same angle θ , we can perform an average over them and compute

$$\Sigma^{ij}(\theta) \equiv \langle \Sigma^{ij}(\Delta \mathbf{k}) \rangle_{\Delta \mathbf{k} = \Delta k} \quad (24)$$

3.2 Normalization

The quantity $\Sigma^{ij}(\theta)$ is not exactly equal to $C(k_i, k_j, \theta)$, because there is a subtle double counting effect which is purely geometrical, and which needs to be cancelled. To see how this arises, we work out a very simple scenario, in which the density field is perfectly isotropic. In that case, we can write $\Delta P(\mathbf{k}) = \Delta P(k)$, hence the angular integration in [Eq.20] is straightforward and we get:

$$\Delta \xi_i(\mathbf{x}) = \Delta \xi_i(x) = \frac{k_i^2}{\pi L} \Delta P_i(k) j_0(k_i x) \quad (25)$$

with $j_0(x)$ being the zeroth order spherical Bessel function. We have also assigned $\delta k = 2\pi/L$ to the shell thickness, which corresponds to the resolution of a simulation of side L . Then, [Eq.18] becomes

$$\Sigma^{ij}(\theta) = \left(\frac{k_i k_j}{\pi L} \right)^2 \Delta P(k_i) \Delta P(k_j) F^{ij}(\theta) \quad (26)$$

where

$$F^{ij}(\theta) = \int j_0(k_i x) j_0(k_j x) j_0(\theta x) x^2 dx \quad (27)$$

The function $F(k_i, k_j, \theta)$ is independent of the actual power spectrum; it is purely a geometrical artefact that corresponds to the counting of the different combinations of $\mathbf{k}_{i,j}$ that produce a given $\Delta \mathbf{k}$. As the former increase, so does the surface of the k -shells, hence there are more ways to fit $\Delta \mathbf{k}$. In the case of an exactly isotropic power spectrum, the results should have no angular dependence. We thus define a normalization $\Sigma_N^{ij}(\theta)$, as the output of [Eq. 24] with $\Delta P(k_{i,j}) = 1$ everywhere on the shells. The final results are obtained by dividing off this normalization, which cancels off the geometrical effect:

$$C(k_i, k_j, \theta) \equiv \frac{\Sigma^{ij}(\theta)}{\Sigma_N^{ij}(\theta)} = \langle \Delta P(k_i) \Delta P(k_j) \rangle \quad (28)$$

We stress again that this result is an average over all configurations satisfying $\mathbf{k}_j = \mathbf{k}_i + \Delta \mathbf{k}$.

To summarize, here is a condensed list of the steps taken to measure $C(k, k', \theta)$:

- (i) Measure the mean angle averaged $\tilde{P}(k)$ from an ensemble of simulations,
- (ii) Select a combination of shells $k_{i,j}$ to cross-correlate,
- (iii) For each simulation, compute $P(\mathbf{k})$, duplicate and multiply each replica by a top hat $u_{i,j}(k)$, which effectively sets to zero every off-shell grid cells,
- (iv) Subtract $\tilde{P}(k)$ from each cell in the shell,
- (v) Fourier transform both grids, complex multiply them, and Fourier transform back to k -space,
- (vi) Loop over the $\Delta \mathbf{k}$ available, bin into $\Sigma(|\Delta \mathbf{k}|^2)$, and express the results as a function of θ ,
- (vii) Repeat steps (v-vi), but this time assigning the value of each cell in the shell to unity, and divide $\Sigma(\theta)$ by this normalization. This is a measure of $C(k_i, k_j, \theta)$ from one simulation,
- (viii) Repeat for all simulations, then compute the mean,
- (ix) Iterate over steps (ii-viii) for other shell combinations.

To achieve better results, we make use of the fact that $P(-\mathbf{k}) = P(\mathbf{k})$, hence, following [Eq.17], we can write $\Sigma^{ij}(-\Delta \mathbf{k}) = \Sigma^{ij}(\Delta \mathbf{k})$.

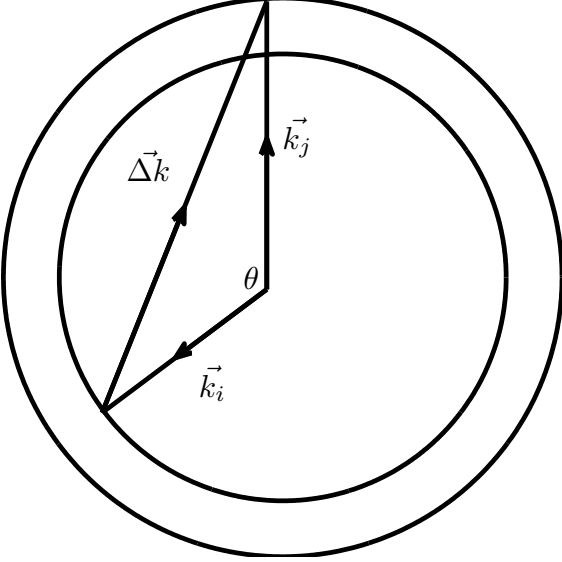


Figure 1. Geometry of the system. For a fixed pair of shells, the magnitudes of the Fourier modes k_i and k_j are fixed, so the angle between them is directly found from the separation vector $\Delta\mathbf{k}$. Note that we use interchangeably numbers or roman letters to denote individual Fourier modes.

This translates into a theoretical symmetry about $\theta = \pi/2$ in the angular dependence of the covariance. That property turns out to be very useful for reducing the numerical noise, since we can measure the covariance over the full angular range, but fold the results on to $0 < \theta < \pi/2$. Also, to avoid interpolating error, we choose to bin in $(\Delta k)^2$ before transforming to θ .

3.3 Zero-lag point

It is important to note that for a given realization, the point at $\theta = 0$, which we refer to as the *zero-lag* point, must be treated with care. When the two shells are identical, i.e. $i = j$, the zero-lag point of each simulation first computes the square of the deviation of the mean $P(k)$, then averages the result over the whole shell. It is equivalent to calculating the variance over the shell, but using a mean which is somewhat off from the actual mean on *that* shell. That effectively boosts the variance. When we average over all simulations, the zero-lag points can be written as:

$$\Sigma^{ii}(0) = \langle P_i^2(\mathbf{k}) \rangle_{N,\Omega} - \langle P(\mathbf{k}_i) \rangle_{N,\Omega}^2 \quad (29)$$

where, in the first term, the angle average and mean over all realizations are computed *after* squaring each grid cell. By comparison, the variance on angle averaged power spectra would be obtained by performing, in the first term, the angle averaging first, then taking the square, then taking the mean.

When the two shells are different, the zero-lag point is now the average over $\Delta P(\mathbf{k})\Delta P(\mathbf{k}')$ on both shells. Since we are no longer squaring each terms, it now includes negative values, hence is generally of much smaller amplitude.

4 VALIDATION OF THE METHOD

We describe in this section a series of tests that compare our numerical results to semi-analytical solutions. We apply our method on a few simple situations in which we control either the density field

or the three-dimensional power spectrum. We first test our recipe on a power spectrum that is set to the second Legendre polynomial. The outcome can be compared to semi-analytical calculations and gives a good grip on the precision we can achieve. We next measure the angular dependence of the covariance matrix of white noise densities and present an estimate of the non-Gaussian Poisson error². We finally measure the angular cross-correlation from Gaussian random fields in order to better understand departures from Gaussianity.

4.1 Testing $C(k, k', \theta)$ with a Legendre polynomial

As a first test, we enforce the z -dependence of the power spectrum to be equal to the second Legendre polynomial, and then compare our results to semi-analytic predictions. We manually set $P(\mathbf{k}) = k_z^2$, which is thus constant across the $x - y$ plane. The mean and the deviation from the mean on a shell k_i are given by $\langle P(\mathbf{k}) \rangle_\Omega = k^2/3$ and $\Delta P(\mathbf{k}) = (2/3)k^2 P_2(\mu)$ respectively, where $P_\ell(x)$ is the ℓ -th Legendre polynomial and μ is the cosine of the inclination angle. The mass auto-correlation function associated with this power is

$$\Delta\xi_i(x) = \frac{-2k_i^4}{6\pi L} j_2(k_i x) \quad (30)$$

The angular dependence of the covariance can be calculated semi-analytically from [Eq. 18] and [Eq. 30]. The angular integration is straightforward, and we obtain

$$\Sigma^{ij}(\Delta k) = \frac{4k_i^4 k_j^4}{9\pi L} \int_0^\infty j_2(k_i x) j_2(k_j x) j_0(\Delta k x) x^2 dx \quad (31)$$

We perform the x integral with $k_{i=j} = 1.0h\text{Mpc}^{-1}$, repeat the procedure for $\Sigma_N^{ij}(\Delta k)$, and obtain a semi-analytical prediction: $C(k, k', \theta) \sim P_2(\cos\theta)$, up to numerical noise. This agrees well with the numerical results produced by our technique, as shown in the top part of Fig. 2. We are plotting the angle dependence of the covariance matrix, normalized by the angle average of the covariance, such that the curve represents the actual cross-correlation coefficient between the Fourier modes. We mention here that in the case where $k_i \neq k_j$, which we encounter in the following sections, we normalize to the square root of the product of the corresponding matrix elements:

$$r(k_i, k_j, \theta) = \frac{C(k_i, k_j, \theta)}{\sqrt{C(k_i, k_i)C(k_j, k_j)}} \quad (32)$$

In the particular case under study in this section, the Fourier modes separated by small angles are strongly correlated by construction.

4.2 Testing $C(k, k', \theta)$ with Poisson-sampled random fields

To measure the response of our code to white noise, we produce a set of 200 random density fields, each with the same comoving volume of $200h^{-1}\text{Mpc}$. These are then Poisson sampled with a fixed sensitivity threshold that is chosen such that ~ 8000 peaks are counted on average. The standard deviation in the measured $P(k)$ decreases roughly as k^{-2} , expected from the fact that the number of cells on a k -shell grows as k^2 .

Because of the random nature of Poisson densities, the variance on a given shell should be roughly constant across all directions. Moreover, after averaging over many realization, Poisson

² See Cohn (2006) for a discussion on different types of noise in a cosmological context.

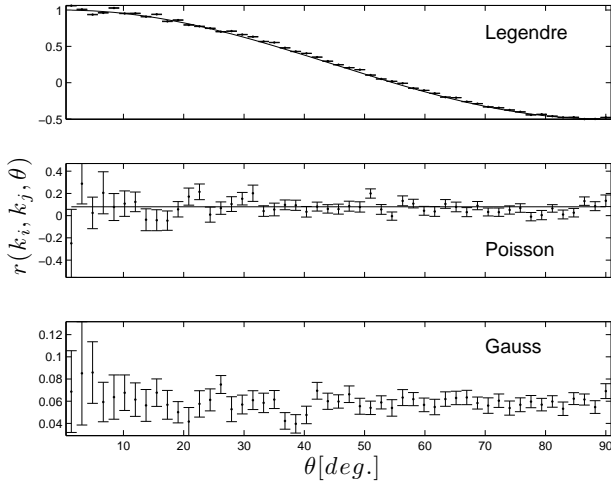


Figure 2. (top:) Angular dependence of the covariance of a power spectrum set to the 2nd Legendre polynomial, calculated here at $k_{i=j} = 1.0h\text{Mpc}^{-1}$. The solid line is the semi-analytical prediction. The curve is normalized to the value of the zero-lag point, such that it represents the actual cross-correlation coefficient between the Fourier modes. In this case, modes that point in like-directions are strongly correlated. (middle :) Angular dependence of the power spectrum cross-correlation coefficient measured from 200 Poisson sampled random fields. The error bars are obtained by 500 bootstrap resampling. We have selected two k -shells i, j that are off by one grid cell: $k_j = k_i + \delta k$, with $\delta k = 0.0314h\text{Mpc}^{-1}$ and $k_i \sim 1.0h\text{Mpc}^{-1}$. The distribution for $i = j$ is similar in shape, except for the zero-lag point, which is much larger than any other points, and the plateau that is slightly higher. The solid line in this figure is the predicted value, which is well within the error bars. We have reproduced a similar plot for Poisson densities with 8.0 million peaks, which is also flat, and find that the height of the plateau scales roughly as $1/n^2$, where n is the number of Poisson sampled objects. (bottom:) Angular dependence of the power spectrum cross-correlation coefficient, measured from 200 Gaussian random fields, this time with $k_j = k_i + 5\delta k$, and again $k_i \sim 1.0h\text{Mpc}^{-1}$. The theoretical prediction is zero, whereas we measure a constant 6 per cent correlation bias across all angles. We have verified that this bias is scale independent by changing $k_{i,j}$.

densities are in principle statistically isotropic. We thus expect the measured angular dependence of the covariance to be very close to flat, and, from [Eq.28], we estimate it should plateau at a value somewhat similar to $C(k, k')$:

$$C_{\text{Poisson}}(k, k', \mu) \sim C_{\text{Poisson}}(k, k') + A\delta_{kk'}\delta_{\mu\pm 1} \quad (33)$$

where the two delta functions ensure that modes with different directions or scales do not couple together. The constant A is much larger than $C_{\text{Poisson}}(k, k')$, for reasons explained in section 3.3, but the precise value is irrelevant to the current analysis. Fig. 3 shows the cross-correlation coefficient matrix for non-Gaussian Poisson noise. We observe that the angle-averaged modes are correlated by more than 30 per cent between scales smaller than $k = 1.0h\text{Mpc}^{-1}$. The reason for this feature is actually independent of cosmology, even though the matrix has a look very similar to that measured from simulations³. The explanation lies in the fact that each of our Poisson densities do not have *exactly* the same number of objects,

³ It is in fact arguable that such a matrix, constructed from a set of Poisson densities, could have better performances at modelling the ‘true’ non-Gaussian covariance matrix, compared to the naive Gaussian approximation.

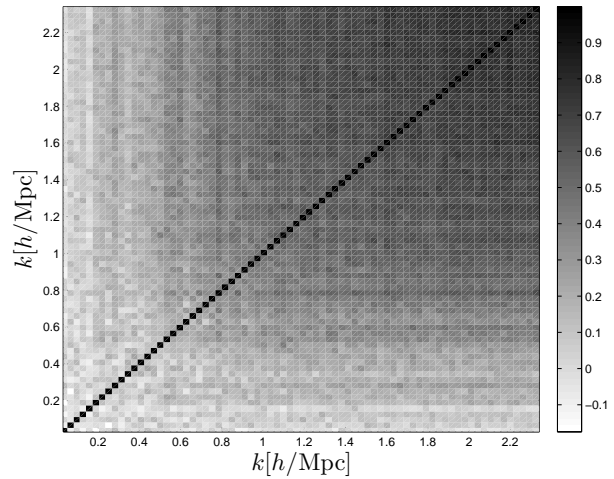


Figure 3. Cross-correlation coefficient matrix, measured from the power spectra of 200 Poisson sampled random density fields, selected to have 8000 peaks on average. The correlation in high k -modes is purely a counting artefact, as explained in the text. This represents our estimate of the non-Gaussian Poisson uncertainty.

hence the asymptotic value of $P(k)$ is not a perfect match for all field. This slight scatter in power translates into a correlation between the high k -modes of a *given* density field. This is in good agreement with the predictions of Cohn (2006), which calculated that the Poisson sampling of Gaussian fields induce non-Gaussian statistics, and that well separated scales can correlate significantly.

We then measure the angular dependence of the covariance for these 200 Poisson distributions, also at $k \sim 1.0h\text{Mpc}^{-1}$. We obtain a distribution that is indeed close to flat, and consistent with a uniform 10 per cent correlation, as shown in the middle plot of Fig. 2. As before, we have normalized the plot such as to exhibit the angular cross-correlation. Because the zero-lag point is typically a few orders of magnitude above the other points, we quote its value in the text or in the figures’ caption where relevant, and resolve the structure of the other angles. The mean of the un-normalized distribution is 133.3Mpc^6h^{-6} , a 10 per cent agreement with our rough estimate. We have re-binned the distributions on to a set of points that are optimal for the upcoming angular integration, as described in section 6.

4.3 Testing $C(k, k', \theta)$ with Gaussian random fields

The next test consists in measuring the angular dependence of the covariance from 200 Gaussian random fields. We use 200 power spectra measured at $z = 0.5$, obtained from N-Body simulations (section 5.1), to generate 200 fields. Similarly to the Poisson fields, we expect the distribution to be overall flat, except for the zero-lag point. Because we choose not to Poisson sample these Gaussian densities, the randomness should be such that near to perfect cancellation occurs between the different angles, and the plateau should be at zero. In the continuous case, the Gaussian covariance can be expressed as

$$C_{\text{Gauss}}(k_i, k_j, \mu) = \frac{2\langle P(k_i) \rangle^2}{N(k_i)} \delta_{ij} \delta_{\mu, \pm 1} \quad (34)$$

where $N(k)$ is the number of Fourier modes in the k -shell. For $k_i = k_j$, the zero-lag point contains perfectly correlated power, so we

expect it to have a very large value. As explained in section 3.3, we cannot directly compare its value to $2P^2(k)/N(k)$, since the former is bin dependent, while the latter is not. In the case where $i \neq j$ however, the zero-lag point should drop down to numerical noise.

The measured angular dependence is presented in the bottom part of Fig. 2, where we see that the distribution is flat and consistent with 6 per cent correlation. This indicates that our method suffers from a small systematic bias and detects a small amount of correlation, in a angle independent manner. We have repeated this measurement for different scales $k_{i,j}$ and obtained the same bias. We therefore conclude that any signal which is smaller than this amount is bias dominated and not well resolved.

5 MEASURING THE ANGULAR DEPENDENCE

In this section, we present our measurements of the angular dependence of the covariance in our 200 simulations. We explore different scale combinations and attempt to compare the outcome to expected results whenever possible. In all figures, the error bars were obtained from 500 bootstrap resampling of our simulations, unless otherwise specified.

5.1 N-body simulations

Since our Universe is not Gaussian at all scales relevant for BAO or weak lensing analyses, a robust error analysis should be based on non-Gaussian statistics, and, as mentioned earlier, N-body simulations are well suited to measure covariance matrices. Our numerical method is fast enough that, for fixed k_i and k_j , we can compute the angular dependence of the covariance matrix in about one minute. The average over 200 realizations can be done in parallel, hence producing all available combinations takes very little time.

The simulations are produced by CUBEP3M (Merz et al. 2005), a public N-body code that is both OPENMP and MPI parallel, which makes it among the fastest on the market⁴. We generate 200 Gaussian distributions of $200 h^{-1}\text{Mpc}$ per side, each with 256^3 particles, starting at $z_i = 40$, and evolve them until $z = 0.5$. The simulations are run on the CITA Sunnyvale cluster, a Beowulf cluster of 200 Dell PE1950 compute nodes, each equipped with 2 quad cores Intel(R) Xeon(R) E5310 @ 1.60GHz processors. Each node has access to 4GB of RAM and 2 gigE network interfaces. The power spectrum of these simulations is shown in Fig. 4, and shows a good agreement with the non-linear predictions from CAMB (Lewis et al. 2000), up to $k \sim 0.25h\text{Mpc}^{-1}$. Beyond that scale, the structures are underestimated due to the resolution limit of the simulations. For the rest of this paper, we only consider well resolved scales, in occurrence those in the range $k \in [0.314, 2.34]h\text{Mpc}^{-1}$, which we organize into 75 linearly spaced bins.

5.2 Results

We present in Fig. 5 and 6 the angular dependence of the covariance between the power spectrum of various scales. As explained in the previous section, the distributions are normalized such as to represent the cross-correlation coefficient between modes separated by an angle θ . In the first figure, both scales are selected to be identical, and vary progressively from $k = 0.17h\text{Mpc}^{-1}$ to $2.34h\text{Mpc}^{-1}$. Modes separated by an angle larger than 30° are less correlated at

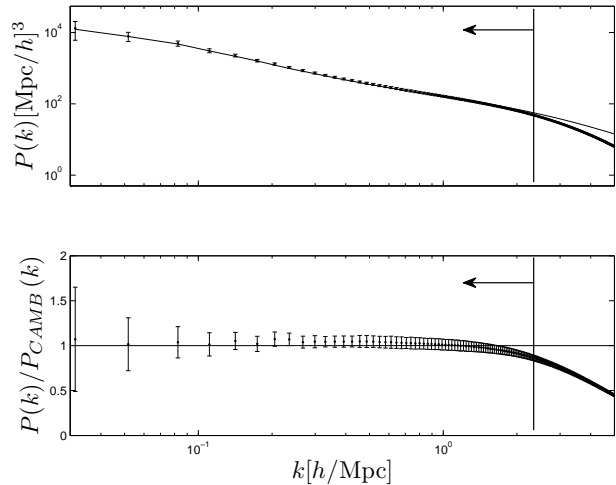


Figure 4. (top:) Power spectrum of 200 simulations, produced by CUBEP3M, compared to CAMB at $z = 0.5$ (solid line). The error bars are the 1σ standard deviation on the 200 measured $P(k)$. We only include modes with $k \leq 2.34h\text{Mpc}^{-1}$ in this analysis, as indicated by the arrow in the figure. (bottom:) Ratio between the simulated and predicted power spectra.

all scales, and the correlation is even smaller for modes smaller than $0.5h\text{Mpc}^{-1}$. These latter modes are grouped in larger bins due to the higher discretization of the shells, and ideally one would like to run another set of simulation with larger volumes to have a better resolution on those scales. However, these larger scales have very little impact on the non-Gaussian analysis we are carrying, we therefore do not attempt to improve the situation. For highly non-linear scales, the correlation between modes separated by angles smaller than 10° increases up to 55 per cent.

In the second figure, one of the two scale is held constant, at $k = 0.61h\text{Mpc}^{-1}$, while the other varies over the same range. Modes separated by angles larger than 30° are less than 10 per cent correlated, for all combinations of scales. When the two scales are of comparable size, the correlation climbs up to values between 15 and 20 per cent for angles smaller than 15° .

This angular behaviour is enlightening, as it shows how the error between Fourier modes separated only by a small angle tends to correlate first. Qualitatively, this validates the fact that in non-Gaussian densities, quasi-parallel Fourier modes are probing essentially the same collapsed structures. When the angle is closer to 90° , however, one mode could go along a filament and the other across it, producing only weak correlations. It could thus be possible to construct a highly clustered density in which we could observe an anti-correlation at 90° , provided we are not noise dominated.

This coherent behaviour is a clear sign that the non-linear structures underwent gravitational collapse, and the departure from Gaussianity and white noise is obvious. Another signature of non-Gaussianity is that even in the presence of a small offset between the scales, the small angle correlation has a value higher than those at larger angles, because of the coupling between those scales. Fig. 6 shows this effect.

5.3 From $C(k_i, k_j, \theta)$ to $C(k_i, k_j)$

It is possible to recover the covariance matrix one obtains from the angle averaged $P(k)$ by performing a weighted sum over the

⁴ <http://www.cita.utoronto.ca/mediawiki/index.php/CubePM>

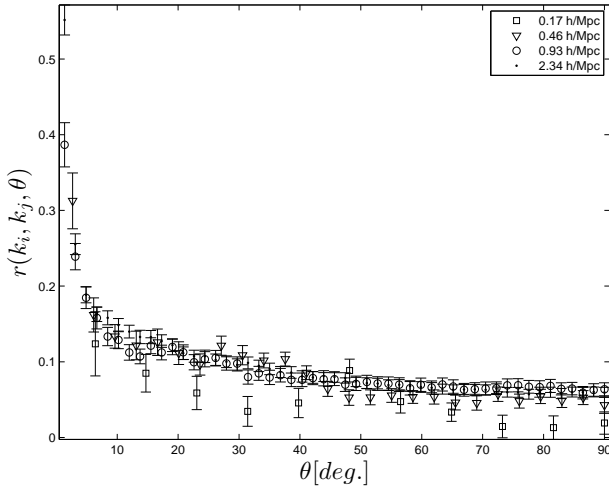


Figure 5. Angular dependence of the power spectrum cross-correlation, measured from 200 density fields, at $k_{i=j} = 0.17, 0.46, 0.93$ and $2.34 h\text{Mpc}^{-1}$. The distribution exhibits a correlation of less than 10 per cent for angles larger than about 30° . For scales smaller than $0.5 h\text{Mpc}^{-1}$, the correlation increases up to 15 per cent for angles smaller than 10° , and to more than 40 per cent for smaller angle.

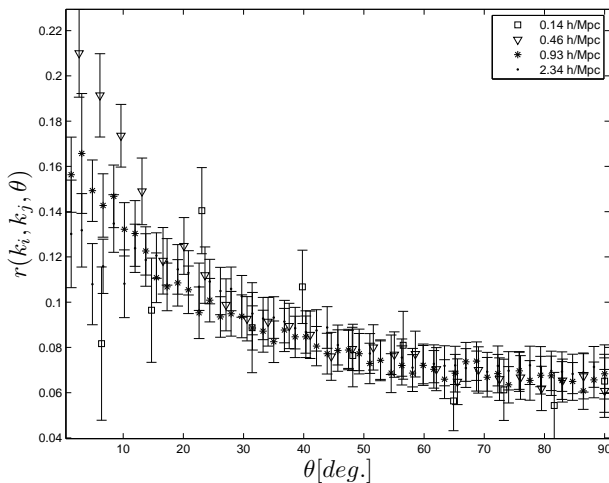


Figure 6. Angular dependence of the power spectrum cross-correlation, measured from 200 density fields, at $k_i = 0.61$, and $k_j = 0.14, 0.46, 0.93$ and $2.34 h\text{Mpc}^{-1}$. The distribution exhibits a correlation of less than 10 per cent for angles larger than about 30° . For scales of similar sizes, the correlation increases up to 15 – 20 per cent for angles smaller than 15° .

angular covariance⁵. Another test of the accuracy of our method is thus to compare the $C(k_i, k_j)$ measured in both ways. This is by far the least convenient way of measuring this matrix, and we perform this check solely for verification purposes.

We perform this weighted sum and construct $C(k_i, k_j)$, then compute a similar matrix from our 200 angle averaged power spec-

⁵ The weights here are simply the number of contribution that enter each angular bin, divided by the square of the total number of cells on the k -shell. In other words, because the angular covariance is an average over many pairs of cells, that average must first be undone, then the different angles are summed up, and we finally divide by the total number of contributions.

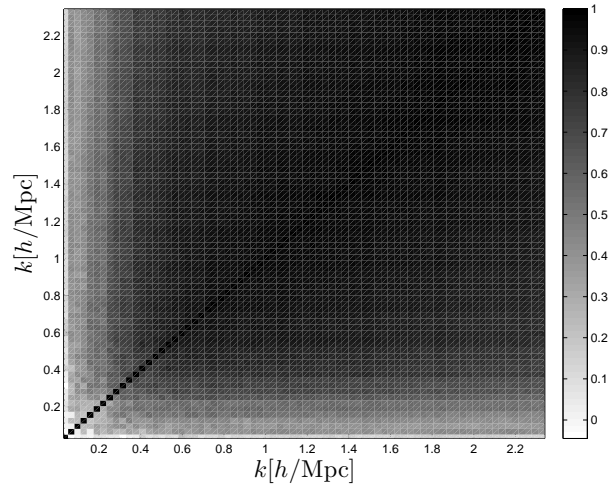


Figure 7. Cross-correlation coefficient matrix, as measured from integrating the angular covariance. Each matrix element i, j was obtained from a reweighted sum over $C(k_i, k_j, \theta)$. This is consistent with matrices previously measured in the literature (Rimes & Hamilton 2005; Takahashi et al. 2009; Ngan et al. 2011)

tra. We present in Fig. 7 the cross-correlation coefficient matrix (see [Eq. 32]) obtained in the first way, and show the fractional error between both methods in Fig. 8. We observe that they agree at the few percent level, so long as we are in the non-linear regime. At very low k -modes, however, many matrix elements are noisy due to the discretization of the shell; the $(\Delta k, \theta)$ mapping in this coarse grid environment becomes unreliable, and the re-weighting hard to do correctly. This results in high fractional errors, but at the same time, this region is still in the regime where the analytic Gaussian prediction is valid. In addition, this paper attempts to solve the bias caused by the non-Gaussianities that lie in the trans-linear and non-linear regime, in which discretization effects are much smaller. Finally, we recall that these matrix elements have very little impact on most parameter studies since such scales contain almost no Fisher information (Rimes & Hamilton 2005; Ngan et al. 2011).

6 MULTIPOLE DECOMPOSITION

As shown in last section, we have extracted the power spectrum covariance matrix $C(k_i, k_j, \theta)$, cross-correlating the 75 different scales selected. Since the final objective is to incorporate this massive object into generic data analysis pipelines, it must be somehow simplified or made more compact. A quick glance at the figures of section 5 reveals that the angular dependence of the covariance can be decomposed into a series of Legendre polynomials, in which only a few multipoles will bear a significant contribution. This allows us to rank the multipoles by importance and to keep only the dominant ones. These results are further simplified in section 7, where we provide fitting formulas to reconstruct $C(k_i, k_j, \theta)$.

In this section, we describe how we perform this spherical harmonic decomposition, then we test our method on the control samples described in section 4, and we finally measure the $C_i(k, k')$ from the simulations.

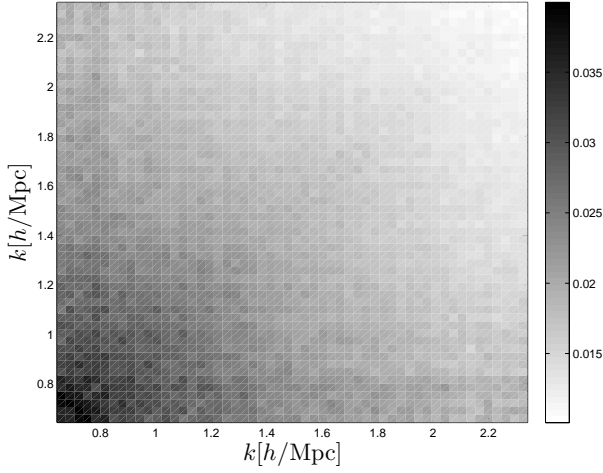


Figure 8. Fractional error between the covariance matrices obtained with the two methods. We have suppressed the largest scales, which are noisy due to low statistics, and present the per cent level agreement at smaller scales. There is a systematic positive bias of about 1.0 per cent in the calculation obtained from the angular integration, which was detected in the Gaussian random field test. The 6.0 per cent correlation that was measured has an even smaller impact after the addition of the zero-lag term.

6.1 From $C(k_i, k_j, \theta)$ to $C_\ell(k_i, k_j)$

Here we lay down the mathematical relation between $C(k_i, k_j, \theta)$ and $C_\ell(k_i, k_j)$. Let us first recall that the spherical harmonics $Y^{\ell m}(\theta, \phi)$ can serve to project any function $F(\theta, \phi)$ on to a set of $a_{\ell m}$ as:

$$a_{\ell m} = \int Y^{\ell m}(\theta, \phi) F(\theta, \phi) d\Omega \quad (35)$$

We substitute $F(\Omega) \rightarrow \Delta P_i(\mathbf{k}) = \Delta P_i(k, \Omega)$, which causes the coefficients to be scale dependent, i.e. $a_{\ell m} \rightarrow a_{\ell m}(k)$. The angular power spectrum at a given angular size $\theta \sim 1/\ell$ is defined as

$$C_\ell(k_i, k_j) \equiv \frac{1}{2\ell + 1} \sum_{m=-\ell}^{\ell} |a_{\ell m}(k_i) a_{\ell m}^*(k_j)| \quad (36)$$

Combining both equations, and writing $C_\ell^{ij} \equiv C_\ell(k_i, k_j)$ to clarify the notation, we get

$$C_\ell^{ij} = \frac{1}{2\ell + 1} \sum_{m=-\ell}^{\ell} \int Y^{\ell m*}(\Omega') Y^{\ell m}(\Omega) \times \Delta P(k_i, \Omega) \Delta P^*(k_j, \Omega') d\Omega d\Omega' \quad (37)$$

We use the completion rule on spherical harmonics to perform the sum:

$$\sum_{m=-\ell}^{\ell} Y^{\ell m}(\Omega) Y^{\ell m}(\Omega') = \frac{2\ell + 1}{4\pi} P_\ell(\cos\gamma) \quad (38)$$

where γ is the angle between the Ω and Ω' directions, and where $P_\ell(x)$ are the Legendre polynomials of degree ℓ . We then write

$$C_\ell^{ij} = \frac{1}{4\pi} \int \Delta P(k_i, \Omega) \Delta P^*(k_j, \Omega') P_\ell(\cos\gamma) d\Omega d\Omega' \quad (39)$$

Since we know that $\mathbf{k}_i + \Delta\mathbf{k} = \mathbf{k}_j$, we make a change of variable and rotate the prime coordinate system such that \mathbf{k} always points towards the z -axis. In this new frame, we have $d\Omega' = d\cos\theta'' d\phi''$, where θ'' is the angle subtended by $\Delta\mathbf{k}$. θ'' thus corresponds to the

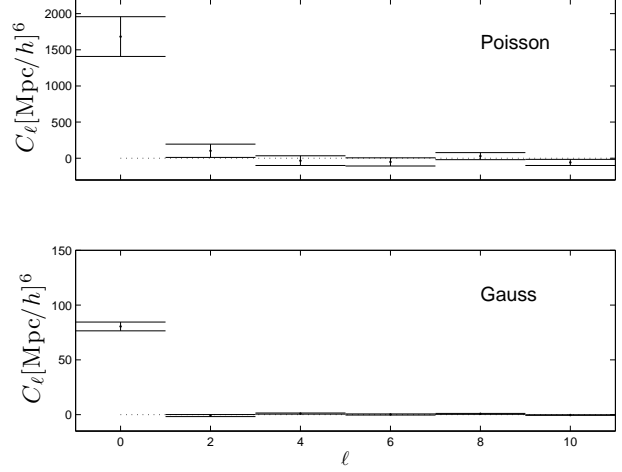


Figure 9. (*top* :) Angular power of the cross-correlation obtained from 200 Poisson densities, at $k_{i-j} \sim 1.0h\text{Mpc}^{-1}$, with an offset of one grid cell between the two scales, corresponding to $\delta k = 0.0314h\text{Mpc}^{-1}$. The power at $\ell \neq 0$ is consistent with zero, as expected from [Eq. 42]. We recall that the angular dependence of the covariance from Poisson densities is very weak, hence it projects almost exclusively on the $\ell = 0$ term. (*bottom* :) Gaussian equivalent at $k_i \sim 1.0h\text{Mpc}^{-1}$, and $k_j = k_i + 5\delta k$. The analytical prediction is zero at all multipole, while we measure a C_0 term of about $80.5h^{-6}\text{Mpc}^6$. This is caused by the 6 percent bias we observed in Fig. 2.

angle between the two Fourier modes \mathbf{k} and \mathbf{k}' . It is also equal to γ in [Eq. 38]. We perform the ‘unprime’ integral first, which gives

$$C_\ell^{ij} = \frac{1}{4\pi} \int P_\ell(\cos\gamma) \int \Delta P_i(\mathbf{k}) \Delta P_j(\mathbf{k} + \Delta\mathbf{k}) d\Omega d\Omega' \quad (40)$$

The inner integral is $C(k_i, k_j, \gamma)$, we rename $\gamma \rightarrow \theta$ and obtain

$$C_\ell^{ij} = \int P_\ell(\cos\theta) C(k_i, k_j, \theta) d\Omega \quad (41)$$

In practice we are dealing with a discretized grid, hence we must convert the integral of [Eq.41] into a sum. To minimize the error, we use a Legendre-Gauss weighted sum, the details of which can be found in the Appendix. In order to validate our method, we designed a few tests that are explained in the following sections.

6.2 Testing C_ℓ with a Legendre polynomial, with Poisson and Gaussian distributions

We start our tests by measuring the $C_\ell(k_i, k_j)$ from the angular dependence of the covariance of power spectra, which is explicitly set to the second Legendre polynomial on the selected k -shells, as described in section 4.1. We expect the projection to produce a delta function at $\ell = 2$, up to numerical precision, since the Legendre polynomials are mutually orthogonal. We observe from this simple test a sharp peak at $\ell = 2$, which is about two orders of magnitude higher than any other points.

We next measure the C_ℓ from the covariance matrix of Poisson densities, whose angular dependence, we recall, is close to flat (see section 4.2), except for the zero-lag point when the two shells are identical. From the orthogonality of the Legendre polynomials, a flat distribution is projected exclusively on the first multipole, we thus expect $C_\ell^{\text{Poisson}}(k \neq k')$ to peak at $\ell = 0$, and to vanish otherwise. Moreover, we expect the $C_\ell^{\text{Poisson}}(k = k')$ to exhibit, in addition, a vertical shift caused by the integration over the zero-lag point. The analytical expression can be obtained from [Eq. 33,41].

The azimuthal integration gives a factor of 2π , the μ delta function gets rid of the last integral, and we get:

$$C_\ell^{\text{Poisson}}(k, k') = \begin{cases} 2\pi C_{\text{Poisson}} \frac{2}{2\ell+1} \delta_{\ell 0} & , k \neq k' \\ 2\pi C_{\text{Poisson}} \frac{2}{2\ell+1} \delta_{\ell 0} + 4\pi A \delta_{kk'} & , k = k' \end{cases} \quad (42)$$

The only scale dependence comes from the surface of the k -shell, and drops as k^{-2} , as explained in section 4.2.

In the $k \neq k'$ case, we find that in the non-linear regime, the $\ell = 0$ point is at least two orders of magnitude above the other even ℓ , and 18 orders above the odd multipoles. The results are presented in the top part of Fig. 9 for $k_{i \sim j} \sim 1.0 h \text{Mpc}^{-1}$. The error bars are obtained from a bootstrap resampling. When $k = k'$, we find that the zero-lag point effectively shifts the whole distribution upwards by an amount equivalent to $4\pi C_{\text{Poisson}}(k, k, 0)$.

Finally, we compare the C_ℓ distribution measured from Gaussian fields to the analytical prediction, obtained from [Eq. 41,34]:

$$C_\ell^{\text{Gauss}}(k, k') = 2\pi \frac{2\langle P(k) \rangle^2}{N(k)} (1 + (-1)^\ell) \delta_{kk'} \quad (43)$$

We measure C_ℓ^{Gauss} from the covariance matrix of 200 Gaussian random fields, as outlined in section 4.3. We show the results in the bottom part of Fig. 9 for the case where there is a slight offset between the two scales. Our results are consistent with zero for all multipoles except $\ell = 0$, which receives an undesired contribution from the constant 6 per cent bias described in section 4.3 and observed in Fig. 2. It turns out that this C_0 contribution is very small (i.e. less than one per cent) compared to the values obtained from simulated density fields, hence we do not attempt to correct for it. In the case where the two shells are identical, we observe similar results, up to an upward shift caused by the zero-lag point, which propagates to all multipoles.

6.3 Measuring $C_\ell(k_i, k_j)$ from simulations

We present in this section the multipole decomposition of the $C(k_i, k_j, \theta)$ matrix measured from our simulations. We show in Fig. 10 the first few non-vanishing multipole moments (i.e. $\ell = 0, 2, 4, 6$), in the case where both scales are exactly equal. All the error bars in this section were obtained from bootstrap resampling. We observe that higher multipoles become closer to the Gaussian prediction given by [Eq. 43], and in fact only the first three differ enough to have a non-negligible impact. As we progress deeper in the non-linear regime, we expect to encounter a mixture of the following two effects: an increase in the number of ℓ required to specify the C_ℓ distribution, or in the departure from the Gaussian predictions of a given multipole. As seen from Fig. 10, the departure between the multipoles and the Gaussian power increases for higher k -modes, an effect prominent in the first multipole. The departure becomes more modest for higher multipoles, and eventually we cannot distinguish between Gaussian and non-Gaussian. This suggests that the non-Gaussianities are encapsulated in the second of the effect above mentioned.

We then show in Fig. 11 the same multipole moments, this time for the case where one scale is fixed at $k = 0.61 h \text{Mpc}^{-1}$, while the other is allowed to vary. Once again, higher multipoles have smaller amplitudes, and approach the null Gaussian prediction. On the diagonal, the relative difference between the multipoles in the linear regime becomes smaller and converge to the predicted value, as expected. In addition, in the linear regime, the angular power of the off-diagonal elements (i.e. $k_i \neq k_j$) is one to two orders of magnitude smaller than the diagonal counter part. As we progress to the

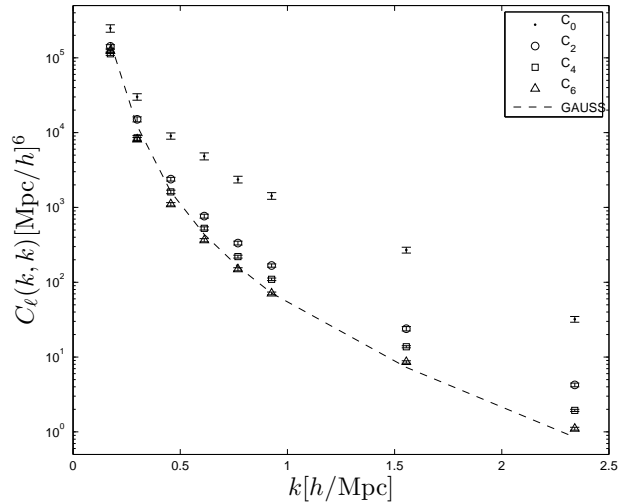


Figure 10. Angular power of 200 densities, where $k_i = j$. The dashed line is the Gaussian prediction, obtained from [Eq. 43]. From this figure, we observe that the diagonals of multipoles higher than $\ell = 4$ converge to the Gaussian predictions.

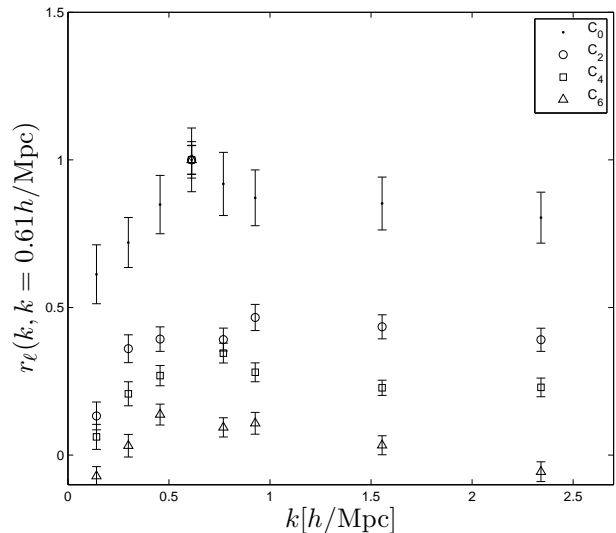


Figure 11. Same as Fig. 10, but with $k_i = 0.61 h \text{Mpc}^{-1}$ being held. The Gaussian prediction is zero in this case. The measurements are normalized by the square root of their diagonal contributions, such as to show the relative importance of each multipole. As ℓ increases, the off-diagonal contribution becomes smaller, even for combinations of scales similar in amplitudes. The fourth point starting from the left is identical to unity for all multipoles, as it corresponds to a diagonal matrix element.

non-linear regime however, the off-diagonal elements decrease less rapidly.

6.4 $C_\ell(k, k')$ matrices

In this section, we organize the results into $C_\ell(k, k')$, and look for the multipole beyond which the off-diagonal elements become negligible. The whole purpose behind this is to model the full covari-

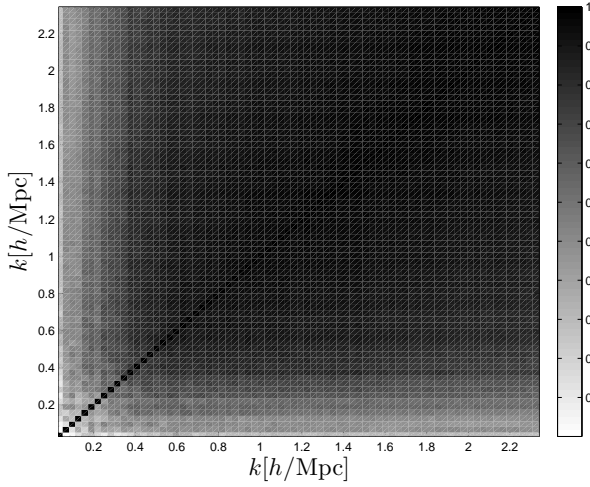


Figure 12. C_0 matrix, normalized such that the diagonal elements are equal to unity. This matrix is completely equivalent to the cross-correlation coefficient matrix of angle averaged $P(k)$. It represents the correlation between different scales, and shows that scales smaller than $k \sim 1.0h\text{Mpc}^{-1}$ are correlated by more than 80 per cent.

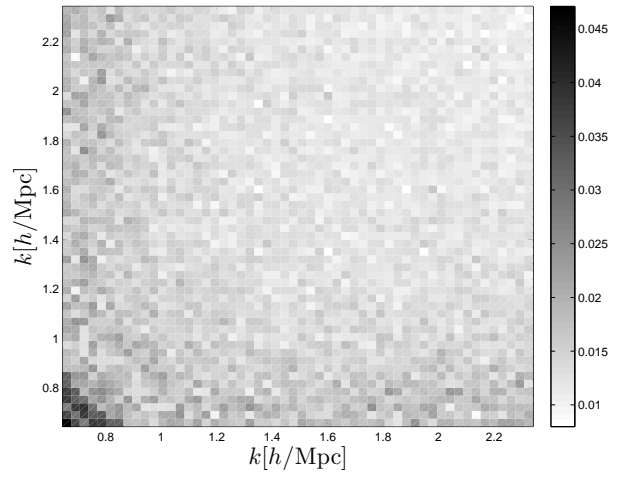


Figure 13. Fractional error between the C_0 matrix and that obtained directly from the angle averaged $P(k)$. We do not show the largest scales, which are noisy due to low statistics and grid discretization. We have also divided the C_0 matrix by (4π) for the two objects to match exactly. We recover the 1.0 per cent bias that is seen in Fig. 8.

ance matrix as:

$$C(k, k', \theta) = \frac{1}{4\pi} \sum_{\ell=0}^{\infty} (2\ell + 1) C_{\ell}(k, k') P_{\ell}(\cos\theta) \quad (44)$$

where the lower ℓ terms are measured from our simulations, and the others obtained from the Gaussian analytical prediction ([Eq.43]).

In the figures of this section, we present these ‘ C_{ℓ} ’ matrices, normalized to unity on the diagonal. These are thus in some sense equivalent to cross-correlation coefficient matrices. Fig. 12 presents the normalized C_0 matrix, which shows a structure similar to that of Fig. 7. The resemblance is not surprising, since $C_0 = 4\pi C(k, k')$. This matrix thus contains the information about the error bars of angle averaged power spectra, as well as their correlation.

By looking at the fractional error between the C_0 matrix and the actual covariance matrix of angle averaged power spectra, we find that our method provides a very good agreement in the trans- and non-linear regimes, down to the few percent level (see Fig. 13). We do not show the largest scales, in which our method is more noisy, for reasons already explained. We recall that an extra contribution to $C_0(k, k')$, not included here, comes from the non-Gaussian Poisson uncertainty, as discussed in section 4.2, and needs to be added in the final analysis.

We now present the next few multipole matrices, and find that beyond $\ell = 4$, very little information is contained in the off-diagonal elements. Fig. 14 shows the C_2 matrix, again normalized to the diagonal for visual purposes. We observe that the smallest scales are correlated up to 60 per cent.

Fig. 15 shows that the correlation in the C_4 matrix is still of the order 50 per cent for a good portion of the non-linear regime. The new feature here is that the strength of the correlation of strongly non-linear modes among themselves starts to decrease as we move away from the diagonal. Fig. 16 shows that C_6 is mostly diagonal. As we progress through higher multipole moments, the off-diagonals become even dimmer, hence do not contain significant amount of new information. From this perspective, a multipole ex-

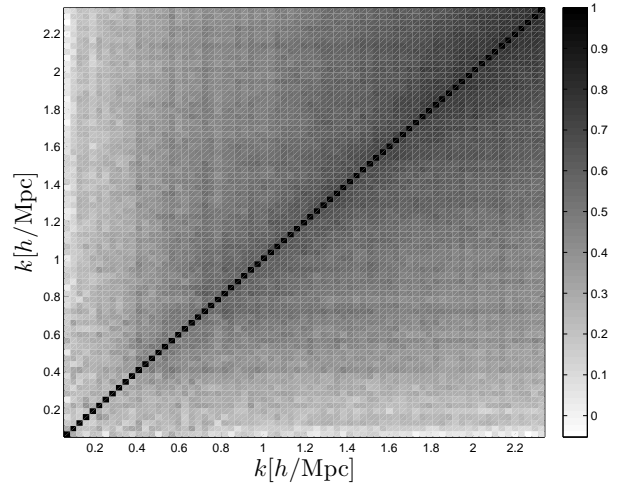


Figure 14. C_2 matrix, normalized such that the diagonal elements are equal to unity. The off-diagonal elements are still correlated at least at 40 per cent for scales smaller than $k = 1.0h\text{Mpc}^{-1}$.

pansion up to $\ell = 4$ is as far as one needs to push in order to model correctly the non-Gaussian features on the off-diagonal elements.

Following [Eq.44], we thus propose to reconstruct the full $C(k, k', \theta)$ from a combination of a) fully non-linear $C_{\ell}(k, k')$ matrices (for $\ell \leq 4$), presented above, b) analytical terms given by [Eq. 43] (which we scale up by 30 per cent as mentioned in section 6.3), and c) non-Gaussian Poisson error, which depends solely on the number density of the sampled fields. In the next section, we decompose and simplify these C_{ℓ} matrices into a handful of fitting functions, and show how one can easily reconstruct the full $C(k, k', \theta)$ at the per cent level precision.

We next present in Fig. 17 the ratio of the diagonal of these matrices to the Gaussian prediction. We observe that all of them are

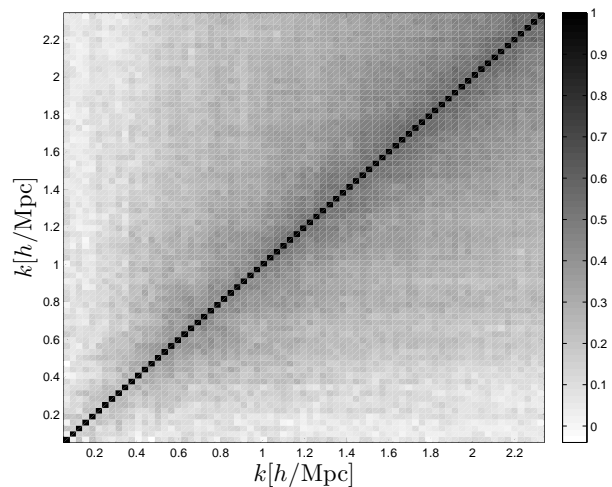


Figure 15. C_4 matrix, normalized such that the diagonal elements are equal to unity. The off-diagonal elements close to the diagonal are correlated at the 30 per cent level in the non-linear regime.

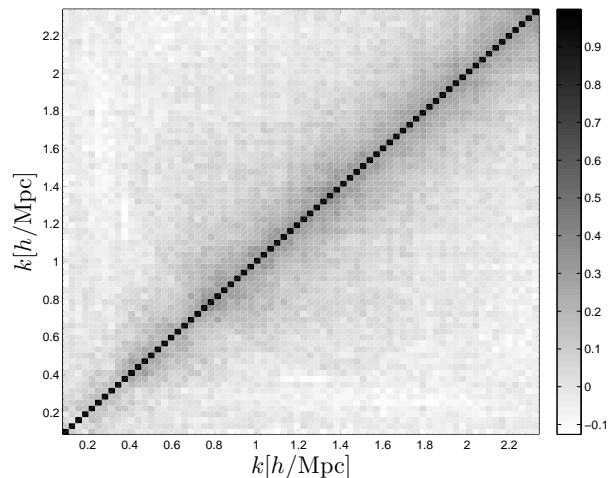


Figure 16. C_6 matrix, normalized such that the diagonal elements are equal to unity. We observe that the matrix is mostly diagonal, and thus decide to treat C_6 and all higher multipoles as purely Gaussian.

consistent with the prediction in the linear regime. As we progress towards the non-linear regime, the largest departure comes from the C_0 matrix, by a factor of about 40 near $k = 1.0h\text{Mpc}^{-1}$. We observe a turn over at smaller scales, which is caused by our resolution limit. We opted not to model it in our fitting formula. C_2 and C_4 mildly break away from Gaussianity by factors of 4 and 2 at the same scale. All the higher ℓ 's are consistent with Gaussian statistics. Over-plotted on the figure are fitting formulas, which are summarized in Table 1.

7 FACTORIZATION OF THE C_ℓ MATRICES

In this section, we simplify even further our results with an Eigenvalue decomposition of the normalized $C_\ell(k, k')$ matrices, as shown

Table 1. Fitting formulas for the ratio between the diagonals of the $C_\ell(k, k')$ and the Gaussian prediction. For all ℓ 's, the function is modelled by $V(x) = 1.0 + (x/\alpha)^\beta$.

ℓ	α	β
0	0.2095	1.9980
2	0.5481	0.7224
4	1.6025	1.0674

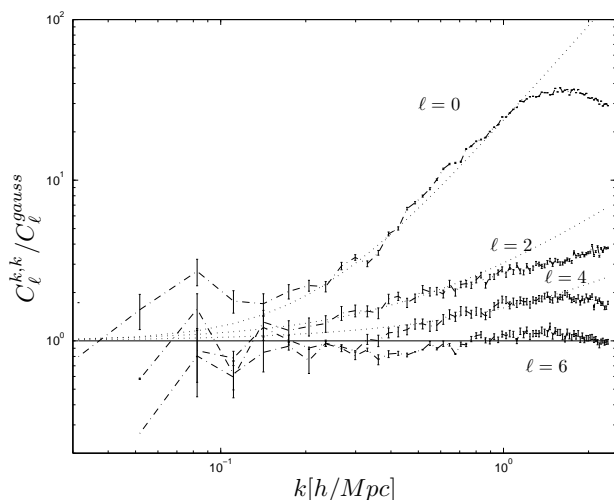


Figure 17. Ratio of the diagonal elements of a few C_ℓ matrices, compared to the Gaussian prediction. The error bars were obtained from bootstrap resampling. Over-plotted are the fitting functions summarized in Table 1.

in the figures of section 6.4. We perform an iterative process to factorize each matrix into a purely diagonal component and a symmetric, relatively smooth off-diagonal part. The later can be further decomposed into a small set of Eigenvectors $U_\lambda(k)$, corresponding to the largest Eigenvalues λ . These are then fitted with simple formulas. Combined with Gaussian predictions and fitting formulas for the diagonal, one can fully reconstruct each of the $C_\ell(k, k')$ matrix, and thus recover $C(k, k', \theta)$ as well.

We start off the iteration by assigning the identity matrix to the diagonal component, which we subtract from the original matrix. We then extract from the remainder the principal Eigenvectors and recompute a new matrix as

$$r_\ell(k, k') \equiv \frac{C_\ell(k, k')}{\sqrt{C_\ell(k, k)C_\ell(k', k')}} = \delta_{kk'} + \sum_\lambda \lambda U_\lambda(k)U_\lambda(k') \quad (45)$$

For the next iterations, we model the diagonal as $\delta_{kk'} - \sum_\lambda \lambda U_\lambda^2(k)$, and decompose the remainder once again. We iterate until the results converge, which takes about 4 steps. We vary the number of Eigenvalues in our iterations, and keep the minimal number for which the reconstruction converges. In the end, the $r_\ell(k, k')$ matrix is modelled as:

$$r_\ell(k, k') = \delta_{kk'}[1 - \lambda U_\lambda^2(k)] + \sum_\lambda \lambda U_\lambda(k)U_\lambda(k') \quad (46)$$

We show in Fig. 18 the fractional error between the original matrix and the factorized one. The factorization of the C_0 matrix with one Eigenvector reproduces the original matrix at the few percent level.

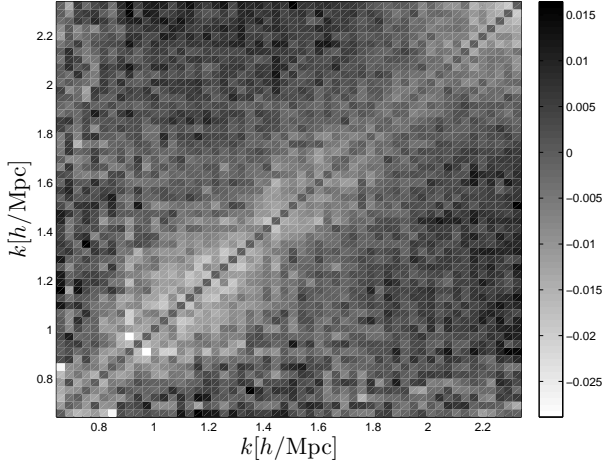


Figure 18. Fractional error between the original C_0 matrix and that produced with the principal Eigenvector. We do not plot the largest scales, which are noisy due to low statistics and grid discretization.

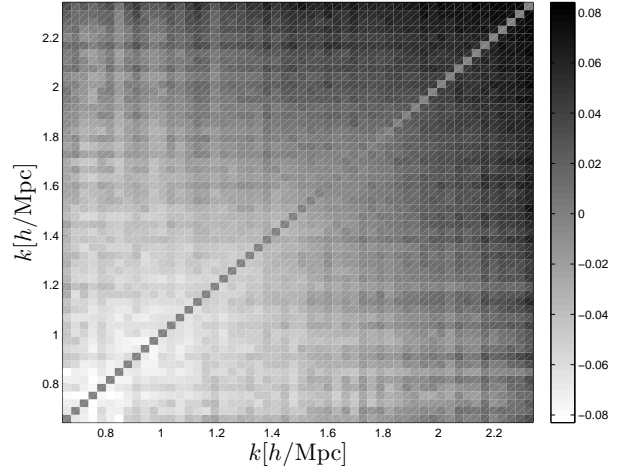


Figure 19. Fractional error between the original C_0 matrix and that produced with the fitting formulas. We do not show the largest scales, which are noisy due to low statistics. The per cent level bias that was seen previously in Fig. 8 is no longer obvious, as the main source of error now comes from fitting the Eigenvector.

The same procedure is also applied for the higher multipoles, in which we have included the first four Eigenmodes, and we find that the fractional error between the reconstructed and the original matrices are also of the order of a few per cent.

We next fit these Eigenvectors with simple functions: for all ℓ 's, the first Eigenvector is parameterized as $U(k) = \alpha \left(\frac{\beta}{k} + \gamma \right)^{-\delta}$, and all the other vectors as $U(k) = \alpha k^\beta \sin(\gamma k^\delta)$. The values of $(\alpha, \beta, \gamma, \delta)$ for the lowest three ℓ 's are presented in Table 2. We require that all these formulas vanish as $k \rightarrow 0$, since the C_ℓ matrices become diagonal in the linear regime. The Eigenvectors of the C_4 matrix are presented in Fig. 20; over-plotted are the fitting formulas. The pixel-by-pixel agreement between the original matrices and those obtained from the fitted formulas is within less than 10 per cent for $k > 0.5$.

Larger scales fluctuate much more as they are less accurately measured, hence the pixel-by-pixel agreement is not expected there. In addition, the matrices with $\ell \geq 6$ are much harder to express with a small set of Eigenvectors, since the Eigenvalues are not decreasing fast enough. In any case, the first three harmonics we provide here contain most likely all the information one will ever use in realistic surveys and forecasts.

7.1 Non-Gaussian Poisson noise

The non-Gaussian Poisson uncertainty, whose construction was presented in section 4.2, can conveniently be incorporated in an analysis by finding the principal Eigenvalue and Eigenvector of $C_0^{\text{Poisson}}(k, k')$. Higher multipoles are not relevant as the angular distribution is flat, as shown in the middle plot of Fig. 2. We test three number densities, corresponding to $n = 5.0 \times 10^{-5}$, 1.52×10^{-4} and $1.0 \times 10^{-2} h^3 \text{Mpc}^{-3}$. In all cases, we decompose the covariance matrix into a diagonal component and a cross-correlation coefficient matrix, find the matrix's principal Eigenvalue and Eigenvector, then fit the latter with: $U_{\text{fit}}^{\text{Poisson}}(k) = \alpha \left(\frac{\beta}{k} + \gamma \right)^{-\delta}$. The diagonal is also fitted with a simple power law of the form

$$V^{\text{Poisson}}(k) \equiv \frac{C^{\text{Poisson}}(k, k)}{C^{\text{Gauss}}(k, k)} = e^\epsilon k^\sigma \quad (47)$$

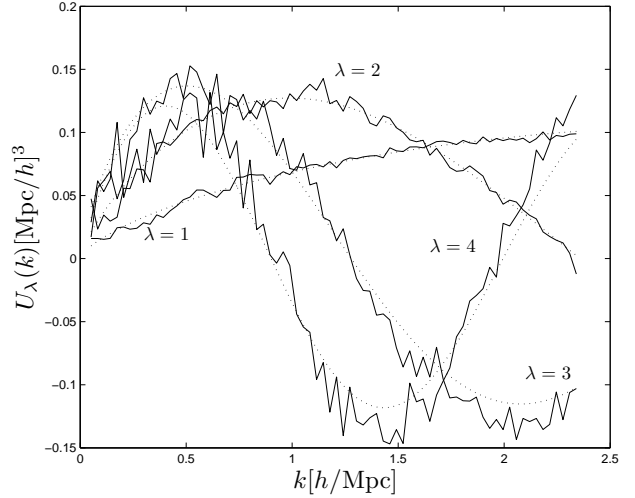


Figure 20. Four principal Eigenvectors of the normalized C_4 matrix (solid lines), and corresponding fitting formulas (dotted lines).

where $C_{\text{Gauss}}^{\text{Poisson}}(k, k) \equiv \frac{p^2_{\text{Poisson}}(k)}{N(k)}$. The best-fitting parameters are summarized in Table 3, and the performance of the Eigenvector fit can be found in the Appendix.

7.2 Recipe

Here we summarize our method to generate accurate non-Gaussian covariance matrices. The full $C(k, k', \theta)$ matrix is then given by [Eq. 44], where the $\ell \leq 4$ terms are obtained from the fitting functions, and the higher multipole moments are obtained directly from [Eq. 43]. The sum over these Gaussian terms can be evaluated analytically as

Table 2. Fitting parameters for the Eigenvectors of the C_ℓ matrices, with their corresponding Eigenvalues. For all ℓ 's, the first Eigenvector is parameterized as $U(k) = \alpha\left(\frac{\beta}{k} + \gamma\right)^{-\delta}$, and all the other vectors as $U(k) = \alpha k^\beta \sin(\gamma k^\delta)$. These parameters were obtained from dark matter N-body simulations, but the method is general, and a different prescription of galaxy population may result in slightly different values.

ℓ	λ	α	β	γ	δ
0	61.9058	0.0501	0.0207	0.6614	2.3045
2	35.7400	0.273	0.8266	1.962	0.816
	4.4144	0.15772	2.4207	0.79153	0.032207
	1.7198	0.14426	4.0613	0.76611	-0.26272
	0.9997	0.14414	5.422	0.84826	0.31324
4	22.0881	0.060399	0.10344	0.64008	2.2584
	4.5984	0.1553	2.3370	0.9307	-0.1154
	2.2025	0.1569	3.6937	0.92304	0.04006
	1.4062	0.15233	5.1617	0.8899	-0.14503

Table 3. Fitting parameters for the diagonal of the $C_0^{Poisson}(k, k')$ matrix, and for the principal Eigenvector of the cross-correlation coefficient matrix. For all three number densities (i.e. $n_{1,2,3} = 5.0 \times 10^{-5}, 1.52 \times 10^{-4}$ and 1.0×10^{-2} respectively), the Eigenvector is parameterized as $U_{fit}^{Poisson}(k) = \alpha\left(\frac{\beta}{k} + \gamma\right)^{-\delta}$, and the ratio of the diagonal to the Gaussian prediction is fitted with $V^{Poisson}(k) = e^\epsilon k^\sigma$. Top to bottom rows correspond to increasing density.

λ	α	β	γ	δ	ϵ	σ
52.02	1.0193	0.0947	2.1021	2.5861	2.6936	2.1347
45.09	0.9987	0.2034	2.1553	2.3407	1.6533	2.1965
24.41	0.2966	3.3736	0.6099	0.6255	-0.4321	2.0347

$$\frac{1}{2} \sum_{\ell=6}^{\infty} (2\ell+1)(1+(-1)^\ell)P_\ell(\mu) = \delta_D(1+\mu) + \delta_D(1-\mu) - 1 - 5P_2(\mu) - 9P_4(\mu) \quad (48)$$

For the non-Gaussian terms, we proceed as follow: each of the normalized $C_\ell(k, k')$ can be constructed from the first set of fit functions $U_\lambda(k)$ provided in Table 2, and following [Eq. 46]. The ‘un-normalized’ $C_\ell(k, k')$ terms are then constructed by inverting [Eq. 32], where the diagonal elements are obtained from the product of the $V_\ell(k)$, also summarized in Table 2. The Gaussian prediction is obtained from [Eq. 43]. In other words:

$$C_\ell(k, k') = \left(\delta_{kk'} \left(1 - \sum_\lambda \lambda U_{\lambda,\ell}^2(k) \right) + \sum_\lambda \lambda U_{\lambda,\ell}(k) U_{\lambda,\ell}(k') \right) \times \sqrt{V_\ell(k) V_\ell(k') C_\ell^{Gauss}(k) C_\ell^{Gauss}(k')} \quad (49)$$

The complete covariance matrix is given by:

$$C(k, k', \mu) = \frac{1}{4\pi} \sum_{\ell=0}^3 (2\ell+1) C_\ell(k, k') P_\ell(\mu) + \frac{2P(k)^2}{N(k)} \left(\delta_D(1+\mu) + \delta_D(1-\mu) - 1 - 5P_2(\mu) - 9P_4(\mu) \right) \quad (50)$$

with $\mu = \cos(\theta)$. This can be written in a more compact form as

$$C(k, k', \mu) = C_{Gauss}(k) \delta(\mathbf{k} - \mathbf{k}') + \sum_{\ell=0}^3 (2\ell+1) \left(G_\ell(k) \delta(k-k') + H_\ell(k, k') P_\ell(\mu) \right) \quad (51)$$

with

$$G_\ell(k) = C_{Gauss}(k) (V_\ell(k) - 1) \quad (52)$$

$$H_\ell(k) = \sum_\lambda \left(F_{\lambda,\ell}(k) F_{\lambda,\ell}(k') - F_{\lambda,\ell}^2(k) \delta(k-k') \right) \quad (53)$$

and

$$F_{\lambda,\ell}(k) = U_{\lambda,\ell}(k) \sqrt{\lambda V_\ell(k) C_{Gauss}(k)} \quad (54)$$

We conclude this section with a word of caution when using the fitting formulas provided here, in the sense that the range of validity of the fit has not been tested on other cosmological volumes. Consequently, we advice that one should limits itself to $k \lesssim 2.0 h \text{Mpc}^{-1}$.

8 MEASURING THE IMPACT WITH SELECTION FUNCTIONS

This section serves as a toy model for a realistic non-Gaussian error analysis, as it incorporates the non-Gaussian covariance matrix measured from N-body simulations with the 2dFGRS selection function (Norberg et al. 2002). We compare the estimated error bars on $P(k)$ between the naive, purely diagonal, Gaussian covariance matrix, the effect of the one-dimensional window function as prescribed by the FKP formalism, the unconvolved non-Gaussian covariance as measured from our 200 N-body simulations, and the convolved non-Gaussian matrix⁶.

We recall that in a periodic volume, a top hat selection function makes the observed and underlying covariance matrices identical. That only occurs in simulated volumes, and in that case, no convolution is necessary. Non-periodicity is dealt with by zero-padding the observed survey, and already results in some coupling between different power spectrum bands. The coupling becomes more important as the selection function departs from a top hat, and in that case, the best estimator of the observed covariance matrix is a convolution of the 6-dimensional covariance over both vectors $(\mathbf{k}, \mathbf{k}')$, given by:

$$C_{obs}(\mathbf{k}, \mathbf{k}') = \frac{\sum_{\mathbf{k}'', \mathbf{k}'''} C_{true}(\mathbf{k}'', \mathbf{k}''') |W(\mathbf{k} - \mathbf{k}'')|^2 |W(\mathbf{k}' - \mathbf{k}''')|^2}{(N^2 N_c \sum_{\mathbf{x}} W^2(\mathbf{x}) w^2(\mathbf{x}))^2} \quad (55)$$

The denominator is straightforward to calculate, while the numerator is a 6-dimensional integral, which must be calculated at all of the 6-dimensional coordinates, a task computationally impossible to perform. For example, with n^3 cells on the grid, we have to sum over n^6 terms for each $(\mathbf{k}, \mathbf{k}')$ pair. There are n^6 such pairs, and each term takes about 3 flop of computation time. For $n = 100$, this process would take $3 * 10^{24}$ flop, and current supercomputers are in the regime of resolving 10^{12} flop per seconds. The above calculation would therefore take about 3000 years to complete. With the factorization proposed in this work however, we break down the computation into smaller pieces and reduce the dimensions to seven at most.

⁶ The code that was used to perform these calculations is made available on www.cita.utoronto.ca/~jharno/AngularCovariance/, and additional explanations can be provided upon request.

Table 4. List of weights $w(\theta, \phi)$ needed for the angular integrals over the selection function. These can be precomputed to speed up the convolution. All integrals are in the form of [Eq. 57].

$\cos^2(\theta)$	$\sin^2(\theta)$	$\cos^2(\theta)e^{\pm 2i\phi}$	$\sin^2(2\theta)e^{\pm i\phi}$
$\cos^4(\theta)$	$\sin^4(\theta)$	$\sin^4(\theta)e^{\pm 2i\phi}$	$\sin^4(2\theta)e^{\pm 4i\phi}$
$\sin^2(2\theta)$	$\sin^2(2\theta)e^{\pm 2i\phi}$	$\sin(\theta)\cos^3(\theta)e^{\pm i\phi}$	$\cos(\theta)\sin^3(\theta)e^{\pm i\phi}$

8.1 Factorization of the 6-dimensional covariance matrix

We break down the true covariance matrix $C(\mathbf{k}'', \mathbf{k}''')$ into a product of simple functions of the form $H_\ell(k'')$, $G_\ell(k'')$ and $P_\ell(\mu)$, where the angular components come exclusively from the Legendre polynomials. Again, μ is the (cosine of the) angle between \mathbf{k}'' and \mathbf{k}''' , and must first be expressed in terms of $(\theta'', \phi'', \theta''', \phi''')$, following [Eq. 14]⁷. The only multipoles that appear in our equations are $\ell = 0, 2, 4$, so μ is to be expanded at most up to the fourth power. For a full factorization, the terms including $\cos(\phi'' - \phi''')$ must further be re-casted in their exponential form with Euler's identities.

When computing the convolution, the first term on the right hand side of [Eq. 51] is spherically symmetric, hence it must be convolved with the selection function as:

$$C_{Gauss}^{obs}(k, k') = \sum_{k''} C_{Gauss}(k'') |W(k'' - k)|^2 |W(k'' - k')|^2 \quad (56)$$

which is pretty much the FKP prescription, namely that the selection function is the only cause of mode coupling.

For the other (i.e. non-Gaussian) terms of [Eq. 51], we use the fact that the only coupling between the \mathbf{k}'' and \mathbf{k}''' vectors comes from the delta function, which couples solely their radial components. This means that all the angular integrations can be precomputed and stored in memory. For example, the only angular dependence in the $\ell = 0$ multipole comes from the selection function itself, hence we can precompute

$$X(\mathbf{k}, k'') = \sum_{\theta'', \phi''} |W(\mathbf{k} - \mathbf{k}'')|^2 \sin(\theta'') w(\theta'', \phi'') \quad (57)$$

and the convolution is now four dimension smaller. The weight function $w(\theta'', \phi'')$ is equal to unity for the C_0 term, and the $\sin(\theta'')$ comes in from the Jacobian in angular integration. For the other multipoles, more terms must be precomputed as well, whose weight functions are summarized in Table 4.

8.2 The 2dFGRS selection function

The 2dFGRS (Colless et al. 2003) is comprised of two major regions, the NGP and the SGP, each of which takes the overall form of a fan of 75×5 degrees, extending from $z = 0.02$ to 0.22 . The selection function is constructed by first integrating the luminosity function $d\Phi(L)/dL$ over all the observed luminosity range, which is both redshift and angle dependent. The results need to be multiplied by the redshift completion function $R(\theta, \phi)$. The parameters that enter this calculations (Φ^* , α and $M_* - 5 \log_{10} h$) are obtained from the 2dFGRS as -1.21 , $1.61 \times 10^{-2} h^3 \text{Mpc}^{-3}$ and -19.66 respectively. The two angular maps ($R(\theta, \phi)$ and $b_J(\theta, \phi)$) required are

⁷ In this section, we use μ instead of $\cos(\theta)$ to denote the (cosine of the) angle between the two Fourier modes, to avoid confusion with θ' and θ'' , which corresponds to the angle of $(\mathbf{k}'', \mathbf{k}''')$ with respect to the x -axis.

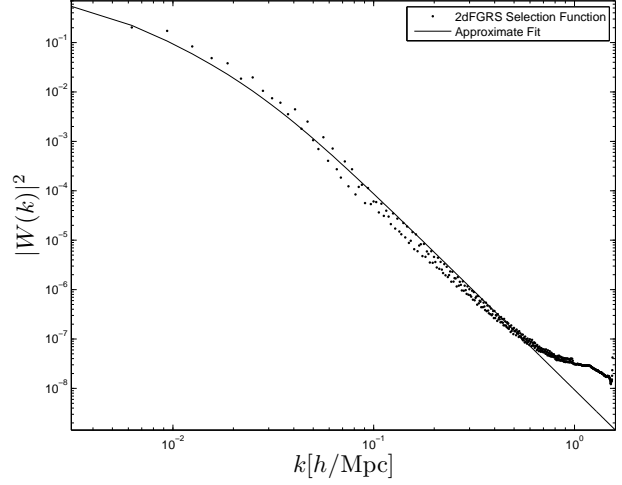


Figure 21. The angle average of the 2dFGRS selection function, compared to an approximate fit provided by Percival et al. (2001). The fit is not perfect as it was obtained with an earlier estimate of the selection function. We also note that our method differs in details with that used in Cole et al. (2005) by the fact that we imposed a cut at redshift of $z = 0.22$, and that we used a somewhat lower resolution.

publicly available on the 2dFGRS website⁸. It is possible to obtain an even more accurate selection function by taking into account the redshift dependence of the magnitude sensitivity, however we do not need such an accuracy for the current work. Finally, our selection function is normalized such that

$$\int |W(\mathbf{k})|^2 d^3 k = 1 \quad (58)$$

To understand the impact of the non-Gaussian Poisson uncertainty on the measured uncertainty, we test various templates, keeping the 2dFGRS selection function fixed. We follow the procedure of section 4.2, with an average number density of $n_{gal} = 1.52 \times 10^{-4} h^3 \text{Mpc}^{-3}$, which corresponds to an early data release of the 2dFGRS data. The final release contains more objects, and has a density of about $n = 5.0 \times 10^{-2} h^3 \text{Mpc}^{-3}$. By comparison, the Poisson uncertainty corresponding to the number count of the Wiggle-Z survey could be modelled with $n = 5.0 \times 10^{-5} h^3 \text{Mpc}^{-3}$ for partial data and about $2.0 \times 10^{-4} h^3 \text{Mpc}^{-3}$ for the final data release. We thus opt for two more number densities: $n = 1.52 \times 10^{-4}$ and $n = 1.0 \times 10^{-2}$.

8.3 Results

We assign the selection function on to a $256 \times 256 \times 128$ grid, where the lower resolution is along the direction perpendicular from the NGP. We recompute the Fourier transform, $W(\mathbf{k})$ and square each terms. Fig. 21 shows a comparison between the angle average of $|W(\mathbf{k})|^2$ and a fitting function provided by the 2dFGRS group.

We then define a second set of bins in spherical coordinates, over which we perform the convolution. For that purpose, we divide the original volume of the survey into 64 radial bins, 48 polar bins and 32 azimuthal bins. The selection function is assigned on the grid by averaging over the 27 closest cells in the original grid. We have included a $\sin(\theta)$ terms in each integrals over the polar angle,

⁸ www.mso.anu.edu.au/2dFGRS/

and a k^2 in each radial integral to properly account for the Jacobian matrix in spherical coordinates.

Fig. 22 shows the diagonal of the convolved covariance matrix, divided by $P^2(k)$, for the FKP prescription and for the progressive inclusion of $\ell = 0, 2$ and 4 multipoles. Also overplotted is the non-Gaussian results without the convolution. We see that already at $k \sim 0.1 h\text{Mpc}^{-1}$, the non-Gaussian fractional error, after the convolution, deviates from the FKP prescription by a factor of about 3.0, while the unconvolved C_0 still traces quite well the FKP curve. This means that the mode mixing caused by the convolution with the survey selection function increases significantly the variance of the observed power spectrum. The departure gets amplified as one progresses towards higher k -modes, and, by $k \sim 1.0 h\text{Mpc}$, the unconvolved C_0 departs from the FKP prescription by almost two orders of magnitudes. Interestingly, the convolved C_0 merges with the unconvolved counterpart at $k \sim 0.5$, where the BAO scale is usually cut off. Inclusion of higher multipole increases the variance by a factor of about 2.0. We have overplotted a simple smooth fitting function of the form :

$$C_{fii}(k) = C_g(k) \left(1 + \frac{2.3}{(0.08/k)^{3.7} + (0.08/k)^{1.1}} + 0.0007 \right) \quad (59)$$

which approximates the contribution from the three lower multipoles.

Fig. 23 shows the convolved cross-correlation coefficient matrix, where the angle average has been taken after the convolution. It is also possible to factorize this matrix, hence we proceed to an Eigenvalue decomposition, following the same iterative procedure as in section 7, solving for the first Eigenvector only. The Eigenvalue was found to be $\lambda = 19.7833$, and we used the sum of a quadratic and a Gaussian function to model the Eigenvector:

$$U_\lambda^{obs}(k) = A \exp\left[-\frac{1}{\sigma^2} \log^2(k/k_p)\right] + (a \log^2(k/k_o) + b \log(k/k_o) + c) \quad (60)$$

with $A = 0.1233$, $\sigma = 1.299$, $a = 0.0049$, $b = 0.0042$, $c = 0.0052$ and $(k_p, k_o) = (0.17, 0.008) h\text{Mpc}^{-1}$ respectively. A comparison of the fit and the actual vector is presented in Fig. 24. The noise reduced cross-correlation coefficient matrix is presented in Fig. 25. We observe that the Fourier modes are already more than 50 per cent correlated at $k = 0.1 h\text{Mpc}^{-1}$, a significant enhancement compared to the unconvolved C_0 matrix, in which the equivalent coupling occurs roughly towards $k = 0.22 h\text{Mpc}^{-1}$. This would most likely have an impact on a non-Gaussian BAO analysis.

9 DISCUSSION

Generally speaking, the departures from Gaussianity will be sensitive to the survey parameters. The quantitative results presented here apply only to the 2dFGRS, however similar calculations could be carried for other surveys. We have found that even for modes of $k \sim 0.1 h\text{Mpc}^{-1}$, the non-Gaussian error bars are higher than those prescribed by the FKP method by a factor of a few, due to mode coupling caused by the convolution of the selection function. This has to be put in contrast with results from pure N-body simulations, which show that the departure from Gaussianity reaches this sort of amplitudes at higher k -modes, as seen from Fig. 22. We also observe that with the 2dFGRS, the non-Gaussian Poisson noise plays an important role if the number density is smaller than $0.01 h^3 \text{Mpc}^{-3}$, but is not enough to characterize all

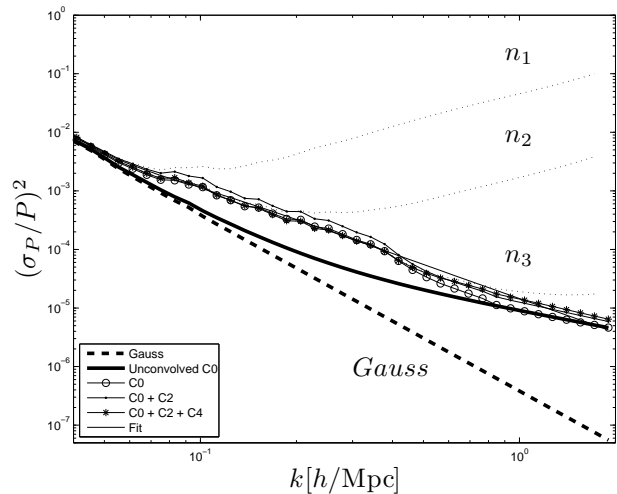


Figure 22. Diagonal of the convolved covariance matrix, first with no multipole, i.e. following FKP prescription (thick dashed line), then with the progressive inclusion of the C_0 (open circles), the C_2 (solid points) and the C_4 multipoles (stars). Also shown is the diagonal of the unconvolved C_0 terms directly measured from N-body simulations (thick solid line), and a fitting function for the total covariance (thin solid line). Finally, the inclusion of the non-Gaussian Poisson noise is represented by three dotted lines, representing the three number density detailed in Table 3. The 2dFGRS final data release has a number density of the order $5.0 \times 10^{-2} h^3 \text{Mpc}^{-3}$, which thus lies between n_2 and n_3 .

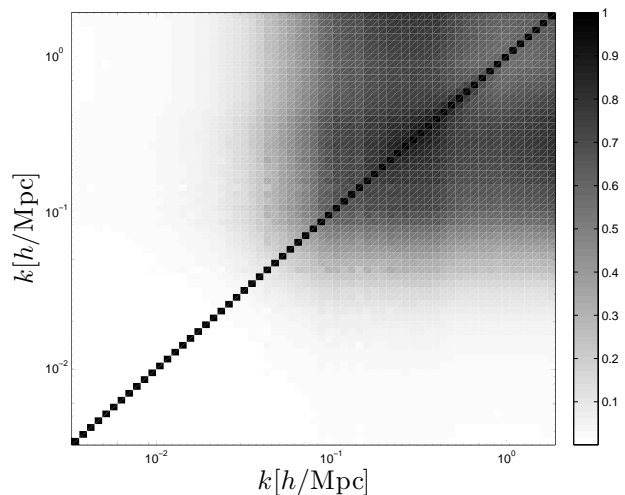


Figure 23. Normalized convolved covariance matrix with all three multipoles.

of the non-Gaussian features of the density field. The C_0 term is the leading contribution of the enhancement observed in the range $k = 0.06 - 0.4 h\text{Mpc}^{-1}$, but for larger k -modes, C_2 and C_4 both play an important role.

In the absence of a survey selection function, significant changes in the covariance matrix do not necessarily translate into noticeable changes in the BAO constraints. For instance, assuming that the BAO mean measurement was performed with a non-Gaussian estimator, the propagation of the non-Gaussian error on to the dilation scale produces constraints that are hardly distinguishable from the naive Gaussian treatment (Takahashi et al. 2011). In

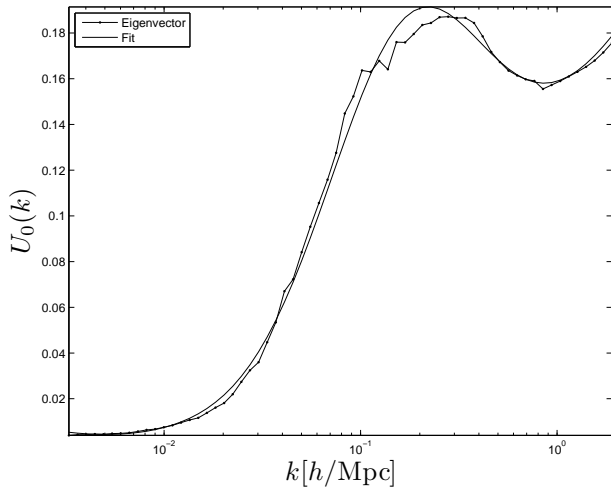


Figure 24. Principal Eigenvector of the convolved C_0 matrix, compared to a simple fitting formula. The fractional error of the fitting function is at most 13 per cent.

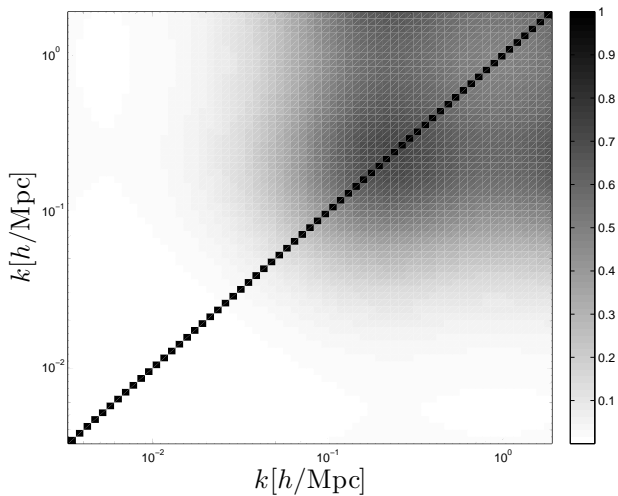


Figure 25. Normalized convoluted covariance matrix with all three multipole, reconstructed from a fit of the principal Eigenvector.

the data analyses however, the estimators of the mean are usually Gaussian, while the power spectrum covariance matrices that enter the calculations are either Gaussian or obtained with mock catalogues. As pointed out previously (Ngan et al. 2011), the estimators constructed in such a way are inconsistent and should be recalculated to include noise in the measured mean. It was found that the corrected – i.e. consistent – error bars are about 10 per cent higher.

It is worth mentioning again that the angle integration of $C(k, k', \theta)$ provides an alternative way to extract the covariance matrix of the angle average power spectra $C(k, k')$. Although the mean value of both methods is identical, i.e. unbiased, the second gives us a better handle on the error on each matrix element, hence provides an optimal measurement of their uncertainty. We have shown in this paper that each matrix element receives its dominant contribution from small angles, while larger angles are noisier. It is thus possible to re-weight the angular integration by taking this new information into account, and obtain more accurate error bars on each

matrix element, compared to the current bootstrap method. As mentioned in the introduction, our next objective in HDP2 is to achieve a similar accuracy with a much lower number of simulations. This would revolutionize the field of observational cosmology as the covariance matrix could be measured internally, i.e. directly from the data.

The techniques presented in this paper call for extensions, as we did not include redshift distortions in our analysis. Also, shot noise will become important when repeating this procedure on haloes, motivated by recent finding that the Fisher information in haloes is also departing from Gaussianity (Neyrinck et al. 2006). It is straightforward to perform a similar analysis with a quadratic halo model, where the halo density is parameterized by $\delta_{halo}(x) = A\delta(x) + B\delta^2(x)$. This involves an extra cross-correlation between the linear and quadratic term, and leaves some room for the choice of A and B , and ultimately, one should work straight from a halo catalogue. The optimal estimator should also be based on a model that is cosmology independent, hence one should compute how the fitting functions scale with Ω_m , ω and z .

As mentioned earlier, the effect of the selection function is enhanced for survey geometries that are different from top-hats, and it would be interesting to repeat some of the BAO data analyses that were performed on such surveys, like the 2dFGRS or Wiggle-Z. The current method also applies to surveys with irregular geometries like those obtained from the Lyman- α forest (McDonald & Eisenstein 2007; McQuinn & White 2011), and we are hoping it will be considered in the elaboration of these future analysis pipelines. In addition, the extraction of non-Gaussian error bars from two-dimensional angular clustering could also be performed with techniques similar to those employed here. We leave it for future work to match our results with predictions from higher order perturbation theory. We would like to verify that the angular dependence we observe in the covariance matrix is predicted by a complete 4-points function analysis, at least in the trans-linear regime.

The results presented in section 6.4 and the recipe presented in the one preceding can find useful applications in the field of weak lensing. Convergence maps, for instance, are constructed from a redshift integral over a past line cone filled with dark matter, weighted by a geometric kernel. Because of the projection nature of this process, the survey maps are sensitive to both large and small scales, where non-Gaussianities have been observed in the convergence power spectrum (Doré et al. 2009).

The lensing fields are quadratic functions of smoothed temperature fields, and the optimal smoothing window function depends not only on the parameter under study, but also on the statistical nature of the sources and lenses (Lu & Pen 2008). Optimal quadratic estimators of lensing fields were first obtained under the Gaussian assumption (Hu & Okamoto 2002; Zahn & Zaldarriaga 2006), then from N-body simulations (Lu et al. 2010), where it was found that the optimal smoothing window function for dark energy involves the first two multipoles of the dark matter power spectrum covariance matrix, $C_0(k, k')$ and $C_2(k, k')$ (see [Eq. 23 – 24] in (Lu et al. 2010)), even in absence of survey selection function. The tools developed in the present paper thus allow one to construct, for the first time and from simple fitting functions, optimal non-Gaussian estimators of dark energy parameters from 21 cm temperature maps.

10 CONCLUSION

Estimating accurately the non-linear covariance matrix of the matter power spectrum is essential when constraining cosmological pa-

rameters including, but not restricted to, the dark energy equation of state ω . So far, many BAO analyses from galaxy surveys were performed under the assumption that the underlying density field is Gaussian, which yields a *suboptimal* measurement of the mean power spectrum and thus of the BAO dilation scale. In addition, and at least as important, the estimated error bars are biased.

To estimate unbiased error bars on the dilation scale is a challenging task, but can now be done. In the simple case of periodic volume, it was shown recently (Ngan et al. 2011) that, first, an unbiased error bar on a suboptimal measurement of the mean could be obtained from the knowledge of the underlying covariance matrix. Second, if one did measure optimally the mean BAO dilation scale, then the optimal measurement of the error requires an estimate of the *inverse* of the power spectrum covariance matrix. This is much more challenging due to the presence of noise, even when dealing with simulations embedded in periodic volumes, but improves the constraining performance by a significant amount.

When estimating the power spectrum and its uncertainty from data, the calculations are more involving since all observed quantities are actually convolved with the survey selection function. The covariance matrix is not isotropic, as it depends on the relative angle between two Fourier modes, hence the convolution cannot be simply factored into two radial components. We are left with a challenging six-dimensional integral to perform, which so far has been an unresolved problem.

In this paper, we present a method to perform this convolution for an arbitrary galaxy survey selection function, and thus allows one to measure unbiased error bars on the matter power spectrum. The estimate is still suboptimal, unless one combines our tools with the PKL formalism. From an ensemble of 200 N-body simulations, we have measured the angular dependence of the covariance of the matter density power spectrum. We have found that on large scales, there is only a weak dependence, consistent with the Gaussian nature of the fields in that regime. On smaller scales, however, we have detected a strong signal coming from Fourier modes separated by small angles. This comes from the fact that the complex phases of these modes are similar, hence they tend to couple first. We next expanded the covariance $C(k, k', \theta)$ into a multipole series, and found that only the first three even poles were significantly different from the Gaussian calculations. We further decomposed these $C_\ell(k, k')$ matrices into diagonal terms and cross-correlation coefficient matrices, from which we extracted the principal Eigenvectors. This allowed us to break down the underlying covariance into a set of Eigenvectors, Eigenvalues plus three diagonal terms. We provided simple fitting formulas for each of these quantities, and thus enable one to construct a full six-dimensional covariance matrix with an accuracy at the few per cent level.

Intrinsically, non-Gaussianities introduce N^2 matrix elements to be measured from N-body simulations, as opposed to N for Gaussian fields. With the proposed method, the number of parameters to measure is reduced to a handful, even if the survey selection function is non-trivial. This factorization is necessary in order to estimate unbiased non-Gaussian error bars on a realistic galaxy survey. We found that in the case of the 2dFGRS selection function, the non-Gaussian fractional variance at $k \sim 0.1h\text{Mpc}^{-1}$ is larger by a factor of three compared to the estimate from the FKP prescription, and by more than an order of magnitude at $k \sim 0.4h\text{Mpc}^{-1}$. With similar techniques, we were able to propagate a few templates of non-Gaussian Poisson error matrices into the convolution and estimate the impact on the measured power spectrum. We showed that with the 2dFGRS selection function, the non-Gaussian Poisson noise corresponding to a number density significantly lower

than $0.1h^3\text{Mpc}^{-3}$ has a large effect on the fractional variance at scales relevant for BAO analyses and should be incorporated in an unbiased analysis.

The cross-correlation coefficient matrix of the convolved power spectrum shows that the correlation propagates to larger scales in the convolution process, and should have a larger impact on BAO analyses for instance. We conclude by emphasizing on the fact that constraints on cosmological parameters obtained from BAO analyses of galaxy surveys are currently significantly biased and suboptimal, but that both of these effects can now be dealt with.

ACKNOWLEDGMENTS

The authors would like to thank Olivier Doré, Ilana MacDonald and Patrick McDonald for useful discussions, Daniel Eisenstein, Martin White and Chris Blake for their comments on early versions of the manuscript, and to acknowledge the financial support provided by NSERC and FQRNT. The simulations and computations were performed on the Sunnyvale cluster at CITA. We also acknowledge the 2dFGRS mask software written by Peder Norberg and Shaun Cole.

APPENDIX A: LEGENDRE-GAUSS WEIGHTED SUMMATION

The conversion of the integral into a sum is performed using a Legendre-Gauss weighted sum (Abbott 2005), in which ℓ ‘collocation’ knots, labeled μ_k with $k = 1, 2, \dots, \ell$, are placed at the zeros of the Legendre polynomial $P_\ell(\mu)$. We choose $\ell = 101$, and we exclude the end points at $\mu = \pm 1$ in order to isolate the zero-lag contribution. The weights w_k are given by:

$$w_k = \frac{2}{(1 - \mu_k^2)(dP_{\ell=101}/d\mu(\mu_k))^2} \quad (\text{A1})$$

This Gaussian quadrature gives an exact representation of the integral for polynomials of degree 201 or less, and provides a pretty good fit to most of our $C(k_i, k_j, \theta)$. In the linear regime, the discretization effect becomes important, and the number of angles one can make between the grid cells drops down as k^2 . In the case were fewer points are available, we choose $\ell = 51, 21, 11$ or 5 , depending on the number of available angular bins. Once we have specified the knots, then, for each scale combination, we interpolate the angular covariance on to these knots, and then perform the weighted sum. As mentioned above, we always treat the zero-lag point separately in order to avoid interpolating its value to the nearest neighbours. We thus break the summation in two pieces:

$$C_\ell^{ij} = 2\pi \sum_{\mu_k \neq \pm 1} P_\ell(\mu_k) C(k_i, k_j, \mu_k) w_k + 2\pi C(k_i, k_j, \mu = 1) \Delta\mu (1 + (-1)^\ell) \quad (\text{A2})$$

The factor of 2π comes from the integral over the ϕ angle, and $\Delta\mu$ is half the distance to the first knot.

APPENDIX B: EIGENVECTOR OF THE POISSON NOISE

This Appendix presents the Eigenvector that best describes the non-Gaussian Poisson noise, as discussed in section 7.1. We restrict ourselves to the case where the number density is the highest, even though similar analyses can be carried for other values of n studied in this paper. We present in Fig. B1 the Eigenvector itself, along

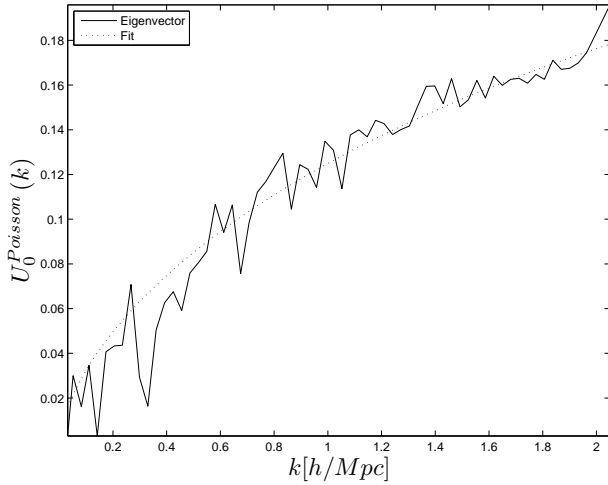


Figure B1. Principal Eigenvector of the cross-correlation coefficient matrix associated with the non-Gaussian Poisson noise, compare to our best-fitting formula.

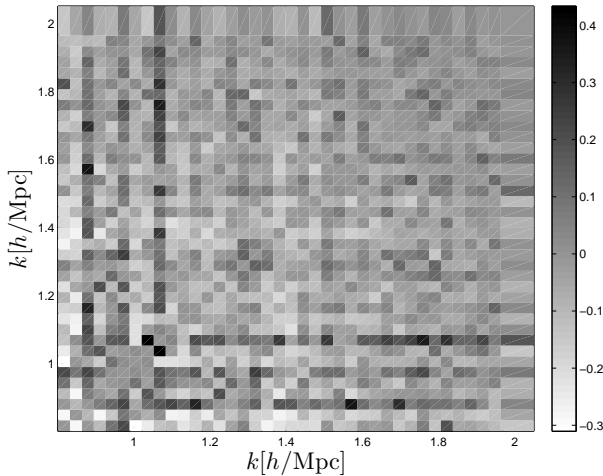


Figure B2. Fractional error between the original cross-correlation coefficient matrix associated with the non-Gaussian Poisson noise, and that constructed with our best-fitting functions. We have not shown the lowest k -modes since these are very noisy.

with the best-fitting formula provided. We next compare the covariance matrix constructed from the fitting functions with the original, and present the fractional error in Fig. B2, which shows an agreement at the per cent level. When compared with the predictions from Cohn (2006), we observe that the overall trends are consistent: first, the Gaussian contribution to the error decreases as one probes smaller scales. Second, densities with lower n see their Gaussian contribution being reduced in the trans-linear regime, where the non-Gaussian Poisson counting becomes more important. Third, densities with lower n produce larger cross-correlation coefficients between trans-linear scales.

REFERENCES

Abbott P., 2005, *Mathematica J*, 9, 689

- Acquaviva V., Hajian A., Spergel D. N., Das S., 2008, *Phys. Rev. D*, 78, 043514
- Albrecht A., et al., 2006, ArXiv e-prints (astro-ph/060959)
- Beaulieu J. P., et al., 2010, in V. Coudé Du Foresto, D. M. Gelino, & I. Ribas ed., *Pathways Towards Habitable Planets Vol. 430 of Astronomical Society of the Pacific Conference Series, EUCLID: Dark Universe Probe and Microlensing Planet Hunter*. pp 266–+
- Benítez N., et al., 2009, *ApJ*, 691, 241
- Bernardeau F., Colombi S., Gaztañaga E., Scoccimarro R., 2002, *Phys. Rep.*, 367, 1
- Blake C., et al., 2010, *MNRAS*, 406, 803
- Blake C., et al., 2011, ArXiv e-prints (astro-ph/1105.2862)
- Chiang L.-Y., Coles P., Naselsky P., 2002, *MNRAS*, 337, 488
- Cohn J. D., 2006, *New Astronomy*, 11, 226
- Cole S., et al., 2005, *MNRAS*, 362, 505
- Coles P., Chiang L., 2000, *Nature*, 406, 376
- Colless M., et al., 2003, ArXiv e-prints (astro-ph/0306581)
- Doré O., Lu T., Pen U.-L., 2009, ArXiv e-prints
- Drinkwater M. J., et al., 2010, *MNRAS*, 401, 1429
- Eisenstein D. J., et al., 2005, *ApJ*, 633, 560
- Feldman H. A., Kaiser N., Peacock J. A., 1994, *ApJ*, 426, 23
- Hu W., Okamoto T., 2002, *ApJ*, 574, 566
- Huchra J. P., Geller M. J., de Lapparent V., Corwin Jr. H. G., 1990, *ApJS*, 72, 433
- Huterer D., 2002, *Phys. Rev. D*, 65, 063001
- Hütsi G., 2006, *A&A*, 449, 891
- Jing Y. P., 2005, *ApJ*, 620, 559
- Lazio J., 2008, in R. Minchin & E. Momjian ed., *The Evolution of Galaxies Through the Neutral Hydrogen Window Vol. 1035 of American Institute of Physics Conference Series, The Square Kilometer Array*. pp 303–309
- Lewis A., Challinor A., Lasenby A., 2000, *Astrophys. J.*, 538, 473
- Limber D. N., 1954, *ApJ*, 119, 655
- LSST Science Collaborations et al., 2009, ArXiv e-prints (astro-ph/0912.0201)
- Lu T., Pen U.-L., 2008, *MNRAS*, 388, 1819
- Lu T., Pen U.-L., Doré O., 2010, *Phys. Rev. D*, 81, 123015
- McDonald P., Eisenstein D. J., 2007, *Phys. Rev. D*, 76, 063009
- McQuinn M., White M., 2011, *MNRAS*, 415, 2257
- Meiksin A., White M., 1999, *MNRAS*, 308, 1179
- Merz H., Pen U.-L., Trac H., 2005, *New Astronomy*, 10, 393
- Metcalfe R. B., White S. D. M., 2009, *MNRAS*, 394, 704
- Neyrinck M. C., Szapudi I., Rimes C. D., 2006, *MNRAS*, 370, L66
- Ngan W.-H. W., Harnois-Déraps J., Pen U.-L., McDonald P., MacDonald I., 2011, ArXiv e-prints (astro-ph/1106.5548)
- Norberg P., et al., 2002, *MNRAS*, 336, 907
- Percival W. J., Cole S., Eisenstein D. J., Nichol R. C., Peacock J. A., Pope A. C., Szalay A. S., 2007, *MNRAS*, 381, 1053
- Percival W. J., et al., 2001, *MNRAS*, 327, 1297
- Peterson J. B., Bandura K., Pen U. L., 2006, ArXiv e-prints (astro-ph/0606104)
- Rimes C. D., Hamilton A. J. S., 2005, *MNRAS*, 360, L82
- Sato T., Hütsi G., Yamamoto K., 2011, *Progress of Theoretical Physics*, 125, 187
- Schlegel D., White M., Eisenstein D., 2009, ArXiv e-prints (astro-ph/0902.4680)
- Takahashi R., et al., 2009, *ApJ*, 700, 479
- Takahashi R., et al., 2011, *ApJ*, 726, 7
- Tegmark M., 1997, *Phys. Rev. Lett.*, 79, 3806
- Tegmark M., et al., 2006, *Phys. Rev. D*, 74, 123507

Vogeley M. S., Szalay A. S., 1996, ApJ, 465, 34

York D. G., et al., 2000, AJ, 120, 1579

Zahn O., Zaldarriaga M., 2006, ApJ, 653, 922

This paper has been typeset from a \TeX / \LaTeX file prepared by the author.